

## **Toward general regime maps for cohesive-particle flows:**

### **Force vs. energy-based descriptions and relevant dimensionless groups**

W. Casey Q. LaMarche, Peiyuan Liu, Kevin M. Kellogg, Aaron M. Lattanzi, Christine M.

Hrenya \*

Department of Chemical and Biological Engineering, University of Colorado, Boulder, CO

#### **Abstract**

Much confusion exists on whether force-based or energy-based descriptions of cohesive-particle interactions are more appropriate. We hypothesize a force-based description is appropriate when enduring-contacts dominate and an energy-based description when contacts are brief in nature. Specifically, momentum is transferred through force-chains when enduring-contacts dominate and particles need to overcome a cohesive force to induce relative motion, whereas particles experiencing brief contacts transfer momentum through collisions and must overcome cohesion-enhanced energy losses to avoid agglomeration. This hypothesis is tested via an attempt to collapse the dimensionless, dependent variable characterizing a given system against two dimensionless numbers: a generalized Bond number,  $Bo_G$ —ratio of maximum cohesive force to the force driving flow, and a new Agglomerate number,  $Ag$ —ratio of critical cohesive energy to the granular energy. A gamut of experimental and simulation systems (fluidized bed, hopper, etc.), and cohesion sources (van der Waals, humidity, etc.), are considered. For enduring-contact systems, collapse occurs with  $Bo_G$  but not  $Ag$ , and vice versa for brief-contact systems, thereby providing support

---

\* Corresponding Author: hrenya@colorado.edu

This is the author manuscript accepted for publication and has undergone full peer review but has not been through the copyediting, typesetting, pagination and proofreading process, which may lead to differences between this version and the Version of Record. Please cite this article as doi: [10.1002/aic.17337](https://doi.org/10.1002/aic.17337)

for the hypothesis. An apparent discrepancy with past work is resolved, and new insight into Geldart's classification<sup>1</sup> is gleaned.

## 1. Introduction

Agglomeration due to short-range, attractive forces between particles is critical to a range of phenomena that span length scales from the planetary to the molecular: formation of the universe,<sup>2</sup> asteroid strength,<sup>3</sup> industrial operations involving solid particles,<sup>4</sup> droplet coalescence,<sup>5</sup> colloid deposition,<sup>6</sup> and atomic aggregation.<sup>7</sup> For flows involving cohesive, solid particles, empirical correlations are known to be unreliable. For example, predictions of entrainment,<sup>8</sup> transport disengagement height,<sup>9</sup> and the size of fluidized agglomerates<sup>10</sup> vary by an order of magnitude or more when applied to the same system.

The state-of-the-art for predicting the behavior of cohesive-particle flows is via regime maps.<sup>1,11-16</sup> One of the earliest and most prolific examples is Geldart's empirical chart of fluidization regimes,<sup>1</sup> with thousands of citations to date<sup>17</sup> despite the lack of significant physical insight. Namely, Geldart's dimensional chart of density difference vs. particle size is system-specific (gas-solid fluidized bed), operating-condition specific (ambient conditions), and cohesion-source specific (van der Waals forces).<sup>1</sup> Some physical insight was shed on this empirical classification by showing that the demarcation of regimes can be recast based on the Bond number – i.e., the ratio of maximum particle-particle cohesive force ( $F_{max}$ ) to particle weight.<sup>11,18</sup> Put another way, the system behavior (macroscopic) was mapped based on particle-particle cohesion levels (microscopic).

Following this preliminary insight, others attempted the micro-macro link in other cohesive systems via dimensionless regime maps based on  $F_{max}$ .<sup>10-15,19,20</sup> The resulting regime maps perform

well for the specific systems and cohesion sources for which they were developed, e.g., predicting the segregation of wet solids in rotating tumblers.<sup>13</sup> Nonetheless, evidence suggests that application to other cohesion sources may be inappropriate. For instance, the link between fluidization behavior and Bond number observed for van der Waals cohesion<sup>11</sup> does not extend to condensed-capillary (humidity-induced) cohesion.<sup>21</sup> Hence, uncertainty remains regarding the applicability of previous regime maps to sources of cohesion different than those used to generate the maps (van der Waals, liquid bridges, etc.).

Here, we seek a more general (and thus more universal) dimensionless group, in which the numerator characterizes particle-particle cohesion and the denominator characterizes the corresponding quantity that acts in opposition (e.g., shear force). Hence, the numerator depends on the source of cohesion (van der Waals, capillary, etc.) while the denominator depends on the specific system considered (sheared, vibrated, etc.). Regarding the numerator, the overwhelming majority of past regime maps have been based on  $F_{max}$ . Nonetheless, the cohesive energy can also be used to quantify the cohesion between particles – i.e., particles agglomerate when their relative kinetic energy ( $KE$ ) is smaller than the critical value of cohesive energy  $KE_{crit}$ <sup>–22</sup> and confusion remains as to which quantity is more relevant in a given situation. For example, numerous estimates for agglomerate size in fluidized systems have been put forth, some of which are based on force balances and others based on energy balances.<sup>10</sup> Further, agglomeration levels have been linked to the cohesive force in some systems<sup>23</sup> and the cohesive energy in others.<sup>24,25</sup> Moreover, even in the same system, the macro-scale behavior has been linked to both  $F_{max}$  and  $KE_{crit}$ . For instance, the flow behavior of a fluidized bed was recently linked to  $KE_{crit}$  for condensed-capillary cohesion,<sup>21</sup> but was previously linked to  $F_{max}$  for van der Waals forces.<sup>11</sup> Finally, the transition of wet solids in a vibrated bed from granular-gas to fluidized-grains was shown to be energy-driven,

whereas the transition from a solid-like bed to fluidized was shown to be force-driven.<sup>26</sup> Though these previous works indicate that the macro-scale behavior was linked successfully to  $F_{max}$  in some cases and  $KE_{crit}$  in others, it is not clear a priori which is more appropriate and why such a distinction exists.

In this work, we resolve the aforementioned discrepancies of cohesive-particle systems via a unifying physical understanding which links the macroscopic (system) behavior to microscopic (particle-particle) interactions. This micro-macro link is demonstrated via experiments and simulations of solids experiencing cohesion from different sources and in a variety of systems that span a range of particle concentrations. Specifically, universal behavior (collapsing of dimensionless plots) is observed using a ratio of forces – the generalized Bond number  $Bo_G$  – for systems dominated by enduring contacts (“dense”) and a ratio of energies – the new Agglomerate number  $Ag$  – for systems dominated by brief contacts or collisions (“dilute”). The numerators of the dimensionless groups depend on the magnitude and type of particle-particle cohesion (microscopic); the denominators characterize the relevant driving force or source of granular energy in the system and thus, unlike the numerators, are system-dependent. A key aspect of this work is the careful attention paid to estimating the denominator of  $Ag$  for each system. Our results support a new physical picture in which  $Bo_G$  dominates in enduring-contact systems, where momentum is transferred via force chains, and  $Ag$  dominates in brief-contact systems, where the flow is dominated by dissipative collisions. Moreover, we contend that Geldart’s force-based classification of fluidized, cohesive solids<sup>1</sup> is more appropriately based on a ratio of energies.

## **2. Development of Dimensionless Groups**

### ***2.1 Numerator considerations: Force vs. energy***

Particle-particle cohesion is often characterized by one of two quantities: the force required to separate surfaces in contact,  $F_{max}$ , or the cohesive potential energy,  $W$ .<sup>27</sup>  $W$  is the integral of the cohesive force  $F_c$  (van der Waals, capillary force, etc.) over the separation distance  $x$ ,

$$W = \int_0^{x_{max}} F_c(x) dx, \quad (1)$$

where the direction of  $x$  and  $F_c$  is between particle centers, and  $x_{max}$  is effectively the maximum distance over which the force acts, i.e.,  $x_{max}$  is set to a finite approximation (that depends on cohesion source) for purposes of practicality and without undue loss of accuracy. The kinetic energy  $KE$  is defined as  $KE = 0.5mv^2$ , where  $m$  is the reduced particle mass and  $v$  is the normal component (taken in the direction between particle centers) of the relative particle velocity. Figure 1 illustrates  $F_c$  and kinetic energy  $KE$  profiles for cohesive particles before and after a collision. As shown in Fig. 1a,  $F_c$  is unaffected by the collisional process. However, even for non-cohesive particles, a fraction of  $KE$  is dissipated during the collision due to its inelastic and/or frictional nature. For cohesive particles, additional energy is lost due to the acceleration of the approaching particles in the cohesive-force field, which leads to a higher impact velocity at contact. As shown in Fig. 1b, such dissipation leads to a hysteresis in  $KE$ . Based on the initial  $KE$  and the amount of dissipation (Fig. 1b), the particles may fully separate after collision (dashed-blue line) or agglomerate (solid-blue line). For frictionless particles, the final  $KE$  of separating particles with normal, relative pre-collisional velocity  $v_i$  is  $KE_f = 0.5mv_f^2 = e^2(0.5mv_i^2 + W) - W$ , where  $e$  is the restitution coefficient and  $v_f$  is the normal, relative post-collisional velocity.<sup>28</sup>  $KE_f$  accounts for both non-contact ( $W$ ) and collisional ( $e$ ) losses in  $KE$ . The demarcation between agglomeration and separation occurs at  $KE_f = 0$ , and can be quantified by the critical agglomeration velocity,  $v_{crit}$  – the minimum, relative (normal), pre-collisional velocity required to avoid agglomeration. The analytical solution for  $v_{crit}$  between inelastic, hard spheres is<sup>22</sup>

$$v_{crit} = (2W(1-e^2)/(me^2))^{1/2}. \quad (2)$$

Here we use  $KE_{crit} = 0.5mv_{crit}^2$ , rather than  $W$ , to quantify the cohesive energy, as collisional losses of  $KE$  play a role in whether or not agglomeration occurs. To underscore the importance of dissipation, note that elastic particles ( $e = 1$ ) always separate due to the absence of dissipation (pre-collision velocity = post-collision velocity), and thus will never agglomerate ( $v_{crit} = 0$ ).

## 2.2 Dimensionless Groups ( $Bo_G$ and $Ag$ )

To determine whether force or energy considerations are more appropriate for a given system, later we will examine plots of the relevant dependent variable for a given system (e.g., degree of agglomeration) versus the level of cohesion. The level of cohesion will be represented by one of two dimensionless groups, one based on force and the other based on energy.  $F_{max}$  and  $KE_{crit}$ , which form the numerators of the respective dimensionless groups, depend on the type of cohesion (van der Waals, etc.) and material properties. The denominators are the system-dependent, characteristic force ( $F_{sys}$ ) and granular energy ( $\theta_{fluc,sys}$ ) driving the flow in the system (described in detail below). Namely, we utilize a generalized Bond number,  $Bo_G$ , which is the ratio of  $F_{max}$  to the characteristic force driving particle motion,  $F_{sys}$ :

$$Bo_G = F_{max} / F_{sys}. \quad (3)$$

We further define a new Agglomerate number,  $Ag$ , as the ratio of  $KE_{crit}$  to the characteristic granular energy  $\theta_{fluc,sys}$  ( $\theta_{fluc,sys} = 3mT_{sys}/2$ , where the granular temperature is  $T_{sys} = \langle \mathbf{v}'^2 \rangle / 3$  and  $\mathbf{v}'$  is the particle velocity relative to the local mean solids velocity):

$$Ag = KE_{crit} / \theta_{fluc,sys} = v_{crit}^2 / 3T_{sys}. \quad (4)$$

It is worthwhile to note that  $F_{max}$  and  $KE_{crit}$ , which form the numerators of the two dimensionless groups, depend on the type of cohesion (van der Waals, etc.) and material properties. The denominators ( $F_{sys}$  and  $T_{sys}$ ), however, are system dependent, as elaborated on

below. Physically, the dimensionless numbers represent a competition between the effects of particle-particle cohesion and the ability of the system to overshadow those effects; small values of  $Bo_G$  and  $Ag$  indicate relatively low levels of cohesion and vice versa.

### **2.3 Denominator considerations: Dependence on system**

Further comment on our choices for the denominators of the two dimensionless groups, and how it relates to past work, is warranted. Namely, particle weight is often used as the denominator<sup>10-12,19,20</sup> for dimensionless groups that utilize a cohesive force in the numerator, though often the physical basis of such a choice is not provided. Accordingly, we choose a more general form of the denominator – i.e., the characteristic force driving the motion ( $F_{sys}$ ). Since dimensionless groups involving  $KE_{crit}$  in the numerator are much less common in past works, the denominator has not been explored as extensively. As noted previously,<sup>24</sup> the kinetic energy of fluctuating particle velocities (or granular energy,  $\theta_{fluc,sys}$ ) is related to the particle impact velocity and hence is relevant to agglomeration; i.e., for impact velocities below  $v_{crit}$ , agglomeration occurs, and vice versa (Figure 1b). However, unlike the particle weight oft used in force-based groups, estimating the characteristic granular energy *a priori* is nontrivial.<sup>10</sup> This challenge may explain why the *mean* kinetic energy was often used in the denominator even though the kinetic energy of *fluctuating* particle motion was previously identified as the relevant choice.<sup>26,29</sup> Unlike  $\theta_{fluc,sys}$ , the *mean* energy of the system is representative of the average velocity of all particles, and therefore does not directly affect agglomeration.

## **3. Methods**

As alluded to above, the appropriateness of a force- or energy-based description of cohesion will be tested via the collapse of plots based on  $Bo_G$  or  $Ag$ , respectively. To ensure

robustness of the results, the dimensional quantities contained in  $Bo_G$  and  $Ag$  must be systematically varied. We accomplished this via experiments and simulations of particles experiencing cohesion from different sources (numerators) and in a variety of systems (denominators). We also considered systems with a wide range of concentrations, in order to test our hypothesis that enduring-contact or “dense” flows are dictated by force considerations and brief-contact or “dilute” flows are dictated by energy considerations. It is worth noting that the dense and dilute classifications defined here are used for conciseness to refer to the nature of contacts only – enduring vs. brief, respectively.

The experiments and soft-sphere DEM (discrete element method) simulations used here are fairly standard and have been documented in our previous publications. For sake of brevity, the details on the experimental and simulation methods are relegated to the supplementary information (Supp Sec S1 – S4). Specifics on the types of cohesion (which affect the numerator of  $Bo_G$  and  $Ag$ ) and systems (denominator of  $Bo_G$  and  $Ag$ ) considered here are detailed below; an overview is provided in Table 1.

### ***3.1 Sources of Cohesion Considered (Numerator)***

We consider cohesion arising from three sources: (i) van der Waals interactions, (ii) capillary bridges formed by condensation (humidity), (iii) and a “square-force” model.<sup>30</sup> These sources, detailed below, impact the values of  $F_{max}$  and  $v_{crit}^2$  (numerators of  $Bo_G$  and  $Ag$ , respectively). Both experiments and discrete element method (DEM) simulations are used to investigate sources (i) and (ii), and only DEM is used for (iii).

Though the values of  $F_{max}$  and  $v_{crit}^2$  are determined based on a given source of cohesion as described below, a few commonalities are worth noting. For both simulations and experiments,  $F_{max}$  occurs at the minimum separation distance,  $x_{min}$ , (and  $F_c(x \leq x_{min}) = F_{max}$ ) which is specific to



the cohesion source. For experiments, the glass particles used are approximately rigid (relatively-high Young's modulus  $E$ ) and therefore we use the (hard-sphere) Eq. 2 for  $v_{crit}^2$ ; see Supp Sec S1 for details on experiments and Supp Sec S2 for details on particles. For simulations, softer particles (smaller  $E$ ) were used and thus  $v_{crit}^2$  was determined from simulations of two-particle collisions (Supp Sec S3) using the force expression  $F_c(x)$  for each cohesion source as described below. The Young's modulus used in different simulations ranged from 1 to  $10^4$  MPa. Since the current work is not intended for directly comparing simulation results against experiments, Young's moduli smaller than that of glass particles ( $E = 7.3 \times 10^4$  MPa)<sup>31</sup> were used in simulations to vary  $v_{crit}^2$  independently of  $F_{max}$ .<sup>32-34</sup> For further details on the particles used in simulations, see Supp S4.

(i) *van der Waals cohesion* – A van der Waals theory validated for the glass particles used in the experiments<sup>35,36</sup> was used to determine  $F_{max}$  and  $v_{crit}^2$  in both experiments and simulations. The cohesive force for two rough spheres with radius  $R$  is given by a “submerged-sphere” model with two scales of roughness:<sup>35</sup>

$$F_{vdW} = \frac{A}{6} \left[ \frac{R}{2(x+2h_l+2h_s)^2} + \frac{2Rr_l}{(R+r_l)(x+h_l+2h_s)^2} + \frac{2Rr_s}{(R+r_s)(x+h_l+h_s)^2} + \frac{r_l}{2(x+2h_s)^2} + \frac{2r_lr_s}{(r_l+r_s)(x+h_s)^2} + \frac{r_s}{2x^2} \right] \quad (5)$$

where  $A$  is the Hamaker constant,  $r_s$  is the small-scale asperity radius,  $h_s$  is the small-scale asperity height,  $r_l$  is the large-scale asperity roughness and  $h_l$  is the large-scale asperity height. A detailed explanation of the submerged sphere method and the modeling of surface via two scales of roughness is available elsewhere.<sup>35,37,38</sup> Our prior work has demonstrated that the two-scale roughness model works well for the glass beads used here, in which two scales of roughness are clearly evident from AFM-based surface maps.<sup>35,36</sup> For both experiments and simulations,  $F_{max}$  is determined via Eq. 5 as  $F_{max} = F_{vdW}(x_{min})$ , where an intermolecular distance of 0.3 nm is used for  $x_{min}$ , thereby precluding an infinite force at contact. For both experiments and simulations,  $x_{max}$  is set to 400 nm in order to determine  $v_{crit}^2$  (via Eq. 1, 2, and 5 for experiments, and via two-particle

DEM simulations for many-particle simulations), which is large enough to not affect  $v_{crit}^2$  appreciably as  $F_{vdw}$  decreases asymptotically with increasing  $x$ .<sup>27</sup> Eq. 5 was also used to determine the van der Waals force as a continuous function of separation distance in the many-particle DEM simulations (along with the particle surface roughness values measured for our experimental materials, which are provided in Table S1 of the supplemental material).

To systematically vary the van der Waals cohesion level, different values of  $F_{max}$  and  $v_{crit}$  (numerators of  $Bo_G$  and  $Ag$ , respectively) were achieved by changing  $A$  in simulations and utilizing different-sized particles in the experiments and simulations (details in Supp Sec S2 and S4).

(ii) *Condensed-capillary cohesion* – The condensed-capillary cohesive force ( $F_{RH}$ ) is determined by solving the system of equations provided in Table 2, where  $RH$  is relative humidity,  $\sigma$  is surface tension, and  $\eta_{RH}$  is the product of ambient air temperature, ideal gas constant and molar density of water; the accuracy and assumptions used for calculating  $F_{RH}$  are discussed elsewhere.<sup>27,39</sup>

In the presence of humidity, small bridges can condense between particles at small separation distances  $x$ . The magnitude of the cohesive force of the bridge is related to the thickness ( $a_2$ ) and curvature ( $a_1$ ) of the bridge, which are found as a function of the half-filling angle  $\beta$ .<sup>42</sup> Similar to the van der Waals force, surface roughness of the particles directly influences the magnitude of  $F_{RH}$  as the liquid bridge condenses between surface asperities. Our previous work showed that the liquid bridge is likely condensing between the small-scale asperities, and hence the bridge curvature and thickness depend on the small-scale asperity radius  $r_s$  in Eq. 8 and Eq. 9 (Table 2).<sup>21</sup> To solve for the condensed capillary force  $F_{RH}$  (Eq. 6 in Table 2), the half-filling angle  $\beta$  (Eq. 8 and Eq. 9 in Table 2) is calculated for a given  $\eta_{RH}$  (Eq. 7),  $RH$  (Eq. 7), and  $x$  (Eq. 8 and

Eq. 9).  $\beta$  is then used to determine the capillary bridge thickness (Eq. 9), which is needed to find the condensed capillary force  $F_{RH}$  (Eq. 6).

This iterative process was used to calculate  $F_{RH}$  in order to determine  $F_{max}$  and  $v_{crit}^2$  for experiments and simulations. In particular, similar to  $F_{vdw}$ , a non-zero  $x_{min}$  (intermolecular distance = 0.3 nm) is required for the vapor molecules to condense into a (liquid) bridge between particles.<sup>43</sup> Accordingly,  $F_{max} = F_{RH}(x_{min})$  is used for both experiments and simulations.  $x_{max}$ , which is needed to determine  $v_{crit}^2$  (Eq. 2), is solved numerically by setting  $F_{RH} = 0$  for the system of equations in Table 2. (For the reader interested in a simpler representation of the relationship between variables, a good approximation of  $x_{max}$  is  $x_{max} \approx 2\sigma/(\eta_{RH} \ln(RH))$  with details discussed elsewhere.<sup>44</sup>)

In order to vary the level of condensed-capillary cohesion, the magnitude of  $F_{max}$  and  $v_{crit}$  (numerators of  $Bo_G$  and  $Ag$ , respectively) were altered by varying the  $RH$  in the experiments and simulations.

(iii) *Square-force model* – The square-force model<sup>30</sup> has similarities to the well-known square-well model,<sup>45</sup> with the key difference being that the cohesive force, rather than the potential energy, is held constant over a short distance from the particle surface, and is zero beyond. Namely, the square-force model is given by,

$$F_{sf}(x) = \begin{cases} F_{max}, & x \leq x_{max} \\ 0, & x > x_{max} \end{cases} \quad (10)$$

where  $F_{max}$  is the constant force that acts over the distance  $x_{max}$  from particle surface.

While no physical analog to the square-force model exists, this model allows  $F_{max}$  and  $v_{crit}^2$  to be controlled independently. Specifically, the cohesive force can be changed while keeping the cohesive energy constant, and vice versa, thereby allowing a clean test as to whether a force-based or energy-based approach is more appropriate for a given system. For example, to keep the force fixed while varying the energy, various  $x_{max}$  values are used for the same  $F_{max}$ , resulting in different

values for  $W$  (and hence  $v_{crit}^2$ ) for each  $x_{max}$  (see Eq. 1 and Eq. 2). The square-force model is only used in DEM simulations and therefore the value of  $v_{crit}^2$  is determined from two-particle simulations as described above and in the supplemental material (Supp Sec. S3).

To systematically vary the level of cohesion in simulations utilizing a square-force model, systems with the same cohesive force ( $F_{max}$ ) but different cohesive energy (numerators of  $Bo_G$  and  $Ag$ , respectively) are examined. Specifically,  $F_{max}$  and  $x_{max}$  are used as controllable input parameters in  $F_{sf}(x)$  (Eq. 10).

### 3.2 Systems Examined (Denominator)

Similar to varying the numerators of  $Bo_G$  and  $Ag$  by changing cohesion sources and their magnitude (Section 3.1), we also varied the denominators by examining different systems. For  $Bo_G$ , determining the denominator (characteristic force driving particle motion; see Eq. 3) is typically more straightforward than for  $Ag$  (characteristic granular energy; see Eq. 4). For the latter, we take the following approach for each system enumerated below: we identify the source of granular temperature (or equivalently granular energy) and estimate its dependency on input parameters. Additionally, the dependent variable (measured or predicted) that we are seeking collapse for is identified below for each system. The dependent variables chosen are necessarily different due to the wide range of systems examined – i.e., the dependent variable in one system may be an input for another (e.g., porosity is an output of the packed bed system but an input to riser flow) and/or the dependent variable in one type of system is non-trivial to define in another (e.g., identifying agglomerates in packed bed). Pictures of the systems are provided in Table 1.

(i) *Simple shear flow (SSF)* – In simulations of SSF, a constant velocity gradient is imposed in one direction.<sup>46</sup> The steady-state fraction of particles in agglomerates ( $N_{agg}/N_{tot}$ , where  $N_{agg}$  is the number of particles in agglomerates and  $N_{tot}$  is the total number of primary particles) is the

dependent variable, which will be plotted against  $Bo_G$  and  $Ag$  for various cohesion levels. First considering the denominator of  $Bo_G$  (Eq. 3), the system-specific driving force for the SSF system is generated from the shear stress, which is proportional to  $\rho_p \gamma^2 d^2$ ,<sup>46,47</sup> where  $\rho_p$  is particle density,  $d$  is particle diameter and  $\gamma$  is shear rate. Since the ratio of system size,  $L$ , to  $d$  is kept constant during the simulations, the characteristic force driving flow is proportional to  $\rho_p \gamma^2 d^4$  and thus we define  $F_{sys}$  as  $\rho_p \gamma^2 d^4$ . Accordingly, based on Eq. 3:

$$Bo_{G,SSF} = F_{max} / \rho_p \gamma^2 d^4. \quad (11)$$

Next considering the denominator of  $Ag$  (Eq. 4), the source of  $\Theta_{fluc,sys}$  is also proportional to shear ( $\propto \rho_p \gamma^2 d^2$ ),<sup>48</sup> and thus we define the characteristic temperature as  $T_{sys} \equiv \gamma^2 d^2$ . Then, according to Eq. 4,

$$Ag_{SSF} = v_{crit}^2 / 3 \gamma^2 d^2. \quad (12)$$

Several points are noteworthy. First, the numerators  $F_{max}$  and  $v_{crit}^2$  depend on the cohesion source (Sec 3.1), but are independent of system, so these quantities will appear in all numerators in this section. Second, subscripts are added to  $Bo_G$  and  $Ag$  to denote the system under consideration, since the denominators are system dependent. Third, note that it is the dependency of  $T_{sys}$  ( $\Theta_{fluc,sys}$ ) on system parameters (inputs) – rather than a specific estimate of this quantity – that is critical. In particular, the significance of specifying the dependence of  $T_{sys}$  on system inputs is important as the usefulness of dimensionless groups stems from a dependency on parameters that are known *a priori* – i.e., input parameters only (rather than local, continuum quantities). Hence, we *define* a characteristic  $T_{sys}$  as  $T_{sys} \equiv f(\text{system inputs})$  (using the symbol  $\equiv$  instead of  $=$ ). Similarly, we define a characteristic force as  $F_{sys} \equiv f(\text{system inputs})$ . This concept is illustrated further in the results (Sec 4). These three comments are similarly applicable to each of the systems described below.

(ii) *Homogeneous cooling system (HCS)* – The HCS simulations are fully periodic with no mean motion or external forces. Thus,  $\Theta_{fluc,sys}$  decays with time.<sup>49</sup> We use Haff's law<sup>49</sup> ( $T = T_0[1+t\zeta_0(0)]^{-2}$  where  $t$  is time,  $T_0$  is the initial granular temperature and  $\zeta_0(0)$  the initial cooling rate<sup>50</sup>) to define  $T_{sys} \equiv T_0/\tau^2$ , where  $\tau$  the dimensionless time  $\tau = (1+t\zeta_0(0))$ .  $F_{sys}$  is the force resulting from the collisional stress (momentum transfer between colliding particles), which stems from granular pressure ( $p_s$ ) in the HCS, namely  $p_s = F_{sys}/a_s$ . Based on the well-documented analogy with molecular gases, we use  $p_s = \rho_p T_{sys}$  along with characteristic  $a_s = d^2$  to define  $F_{sys} \equiv T_0 \rho_p d^2 / \tau^2$  (where the ratio of domain length to particle size,  $L/d$ , is kept constant for all simulations). Therefore, the HCS Agglomerate number is

$$Ag_{HCS} = v_{crit}^2 / (3T_0 / \tau^2), \quad (13)$$

and the Bond number of the HCS is

$$Bo_{G,HCS} = F_{max} / (T_0 \rho_p d^2 / \tau^2), \quad (14)$$

The level of agglomeration,  $N_{agg}/N_{tot}$ , is again the dependent variable of interest.

(iii) *Riser* – The riser is a dilute suspension of particles (solids volume fraction  $\phi = 1\%$ ) entrained by upward-flowing gas in a fully periodic domain. The steady-state agglomeration level  $N_{agg}/N_{tot}$  is taken as the dependent variable. In a riser, the drag force drives the motion of the particles, and it is commonly described by  $F_{drag} = (1/8)C_D \rho_f \pi d^2 (U - u_s)^2$  for single particles,<sup>51</sup> where  $C_D$  is the coefficient of drag,  $U$  is the gas velocity and  $u_s$  is the solids velocity. We use the single particle terminal velocity  $U_t$  (a value that can be determined *a priori*) as an estimate for  $U - u_s$ . Accordingly, the system-specific driving force used here is  $F_{sys} \equiv \rho_f d^2 U_t^2$  and thus the Bond number for the riser is

$$Bo_{G,Riser} = F_{max} / \rho_f U_t^2 d^2, \quad (15)$$

where  $\rho_f$  is the gas density and the single-particle terminal velocity  $U_t$  is used to estimate the relative velocity between phases. For our simulations (homogenous and uniform gas flow),  $\theta_{fluc,sys}$  is generated via the interaction of neighbor particles through the fluid; this source is proportional to the slip velocity squared,<sup>52</sup> i.e.,  $T_{sys} \equiv U_t^2$ . Hence, the riser Agglomerate number is given by:

$$Ag_{Riser} = v_{crit}^2/3U_t^2. \quad (16)$$

(iv) *Bubbling Bed (BB)* – Controlled sedimentation is achieved by incrementally lowering the gas velocity at the bottom of the bed (inlet) until the particles come to rest in a packed-bed state. Prior to each sedimentation run, the gas delivered to the bottom of the bed at a sufficiently high velocity to ensure the bed would be in a bubbling state. This initial gas velocity to ensure the particles were initialized in a bubbling bed (BB) was determined in our previous work.<sup>21,53</sup> Thus, the BB is the (relatively dilute) starting point of our sedimentation system, and it was investigated experimentally.<sup>21,53</sup> The minimum velocity associated with the presence of bubbles  $U_{mb}$ , normalized by the non-cohesive value  $U_{NC}$ ,<sup>39,53</sup> is the dependent variable of interest. When solids are fully fluidized in the bubbling state, the drag equals bed weight, and thus

$$Bo_{G,BB} = F_{max}/mg. \quad (17)$$

Although dilute (collision-dominated), the BB has a much higher concentration than the HCS and SSF, and thus we assume that motion of individual particles is  $\sim d$  between collisions. Accordingly, the potential energy of the relative motion of particles ( $mgd$ ) is used to define  $T_{sys} \equiv 3dg$ , and the Agglomerate number in the BB is thus

$$Ag_{BB} = v_{crit}^2/(3dg). \quad (18)$$

(v) *Packed Bed (PB)* – In the dense, packed-bed (PB) limit of the sedimentation system, no gas flow occurs. The particles are stationary for several gas velocity set points prior to the no-gas-

flow condition.<sup>54</sup> Hence, a granular energy does not exist. Bed compaction is caused by the gravitational forces on the particles, and thus  $F_{sys}$  is  $mg$  and the PB Bond number is

$$Bo_{G,PB} = F_{max}/mg. \quad (19)$$

The porosity  $(1 - \phi)$  is the dependent variable of interest in both experiments and simulations. However, simulations and experiments are considered separately because DEM is limited to smaller beds and particles with a smaller Young's modulus (Sec 3.1) than experiments.<sup>34</sup>

(vi) *Hopper* – Simulated particles are discharged through a slit at the bottom of a hopper. The steady-state discharge rate of cohesive solids ( $D_c$ ) is the dependent variable of interest and is normalized by the discharge rate of non-cohesive particles ( $D_{NC}$ ). Gravity drives flow from the hopper, i.e.,  $F_{sys} \equiv mg$ , and thus the Bond number of the hopper is

$$Bo_{G,Hopper} = F_{max}/mg. \quad (20)$$

Similar to the BB, the Agglomerate number of the hopper is

$$Ag_{Hopper} = v_{crit}^2/(3dg), \quad (21)$$

because the hopper is dense (particle motion limited to  $\sim d$ ) and  $T_{sys}$  is proportional to the potential energy associated with the relative particle motion.

#### 4. Results and Discussion

Below we evaluate our hypothesis that a force-based description is more appropriate when enduring contacts dominate and an energy-based description is more appropriate when contacts are brief in nature. Namely, we use the wide range of experimental and simulation systems (fluidized bed, hopper flow, etc.) and cohesion sources (van der Waals, humidity, etc.) detailed above to see if the dependent variables of dense systems collapse with  $Bo_G$  but not  $Ag$ , and vice versa for dilute systems.



#### 4.1 Validating $T_{sys}$ (input) against $T_{actual}$ (output)

Before testing for collapse with  $Ag (=v_{crit}^2/3T_{sys})$ , it is worthwhile to verify that a correct characteristic granular temperature ( $T_{sys}$ ) was identified for each system based on input parameters alone. Recall that our approach, as detailed above, was to identify the source of granular temperature for each system, and then define  $T_{sys}$  such that it captured the dependency of this source on input parameters. As a quick gauge of the appropriateness of this approach, we can compare this characteristic  $T_{sys}$  based on input parameters to the actual granular temperature observed in the system. This is straightforward to accomplish for DEM simulations only, as experimental measurements of granular temperature are non-trivial at best. Further, because granular temperature is defined in terms of a fluctuation velocity, this comparison is most easily accomplished in systems with well-defined local, mean velocities – i.e., SSF (linear mean velocity) and HCS (zero mean velocity). The resulting comparison between the characteristic  $T_{sys}$  (based on input parameters) and the granular temperature  $T_{actual}$  extracted from simulations (output), is shown in Figure 2 for SSF and HCS (subplots a and b, respectively).  $T_{sys}$  and  $T_{actual}$  are only plotted in Figure 2 when the systems are not fully agglomerated (i.e., when  $T_{actual} > 0$ ), because the definition of granular temperature becomes enigmatic when the systems are fully agglomerated). The nearly linear behavior indicates that the  $T_{sys}$ , identified as the source of granular temperature (denominator of  $Ag$ ) is proportional to the measured value of the granular temperature  $T_{actual}$  except when the system  $T_{actual} \sim 0$ . Not surprisingly, the proportionality constant differs by  $\sim 1$  order of magnitude between SSF and HCS, since  $T_{sys}$  is a characteristic temperature of a given system rather than an estimate of  $T_{actual}$ .

#### 4.2 Collapse of brief-contact (dilute) systems

Author Manuscript

Given the confidence in our approach for determining a characteristic temperature  $T_{sys}$  as described above, we are now well-positioned to begin evaluating our hypothesis that brief-contact (dilute) systems will collapse with  $Ag$  but not  $Bo_G$ . In particular, for a given system, we methodically changed not only type the cohesion, but also other parameters appearing in the numerator and denominator of the dimensionless groups in order to ensure robustness of any observed collapse. Figure 3 displays the results from the first system examined, namely SSF, in which the fraction of particles in agglomerates (dependent variable) is plotted against  $Bo_{G,SSF}$  and  $Ag_{SSF}$  (independent variables) in subplots a and b, respectively. Each data point in these plots represent a different system condition. First, the cohesion source and its associated parameters –  $A$  for van der Waals induced cohesion,  $RH$  for condensed-capillary cohesion, and  $F_{max}$  and  $x_{max}$  for square-force cohesion – were varied such that a wide range of cohesion levels, as quantified by  $F_{max}$  and  $v_{crit}^2$  in the numerators of  $Bo_{G,SSF}$  and  $Ag_{SSF}$ , respectively, were obtained. The Young's modulus was also varied, leading to further changes in  $v_{crit}^2$  values (Supp Sec S3). Moreover, the shear rate and particle diameter, which appear in the denominator of  $Bo_{G,SSF}$  and  $Ag_{SSF}$ , were also varied. Figure 3 contains the results from 63 different SSF simulations. Table S5 contains a complete listing of the system conditions examined (inputs), as well as key output variables for the SSF simulations. Aside from  $Bo_{G,SSF}$  and  $Ag_{SSF}$ , all other dimensionless groups characterizing the SSF system were kept constant: solids fraction  $\phi = 0.05$ , restitution coefficient  $e = 0.97$ , and  $L/d = 13.78$ , where  $L$  is the system length and  $d$  is the particle diameter.

The results plotted in Figure 3 provide preliminary support for the hypothesis that energy-based descriptions are more appropriate for dilute systems. Namely, the fraction of particles in agglomerates in Fig. 3a does not collapse when plotted against  $Bo_{G,SSF}$  (Fig. 3a). However, in Figure 3b, the fraction of particles in agglomerates collapses when plotted against  $Ag_{SSF}$ . Similarly,

for the simulated HCS (Figure 4) and riser (Figure 5), and for the experimental BB (Figure 6), collapse is observed against  $Ag$  but not  $Bo_G$  over a wide range of input parameters. For the simulated dilute systems, i.e., HCS and riser, the cohesive source and magnitude of cohesion were varied by changing the relevant input parameters for each cohesion type: the Hamaker constant for the van der Waals force (Eq. 5), the relative humidity for the condensed-capillary force (Eq. 6), and  $F_{max}$  and  $x_{max}$  for the square force cohesion (Eq. 10). Additionally, the particle properties  $E$  and  $d$  were also varied along with the initial temperature (system condition) in the HCS, resulting in a total of 18 different HCS simulations were investigated, as overviewed in Table S6. For the riser, in addition to changing the parameters influencing the cohesive magnitude –  $F_{max}$  and  $v_{crit}^2$  –  $Bo_{G,Riser}$  and  $Ag_{Riser}$  were manipulated by varying the particle density, Young's modulus, superficial gas velocity ( $U$ ), gas viscosity ( $\mu$ ), for a total of 36 riser conditions that were simulated (Table S7 in supplementary material). The numerator and denominator of  $Bo_{G,BB}$  and  $Ag_{BB}$  were experimentally varied by using glass beads of different size (Supp. Sec. S2) and adjusting the  $RH$ , resulting in BB experiments at 11 different conditions (Table S8 in the supplementary material). Collectively, the collapse of these dilute systems (SSF, HCS, riser, and BB) for  $Ag$  and not  $Bo_G$  provide robust evidence that systems dominated by brief contacts are most appropriately described by energy-based arguments. A plausible physical explanation is as follows: particles experiencing brief collisions must overcome energy losses associated with cohesion to avoid agglomeration (Fig. 1b); such a hysteresis (agglomeration upon impact) cannot be captured by the force profile (Fig. 1a).

It is also noteworthy that the  $Ag$  plots (Figures 3b, 4b 5b, and 6b) in the dilute systems are similar in shape. This similarity can be traced to the transition from non-agglomerating to agglomerating regime occurs when the  $KE$  of particle collisions just balances the  $KE$  dissipated

during collisions. At this transition point, the systems quickly approach a fully agglomerated state ( $N_{agg}/N_{tot} = 1$ ) once agglomeration onsets as the  $KE$  generation becomes smaller than the dissipation.

Despite their similarity in shape, the value of  $Ag$  for which the transition from non-agglomerating to agglomerating occurs varies by orders of magnitude for the different systems (Figures 3b, 4b, 5b, and 6b). Such differences are a result of the denominator of  $Ag$  being expressed in terms of  $T_{sys}$ , a characteristic temperature that is *proportional* to the granular temperature in a given system rather than a direct estimate of its magnitude (Sec 4.1). To further illustrate this point, the granular temperature was extracted from all of the simulated systems (SSF, HCS, and riser) –  $T_{actual}$  – and used in the denominator of  $Ag$  instead of  $T_{sys}$ ; see Figures 3c, 4c and 5c, respectively. The inverse of  $Ag$  is plotted in Figures 3c, 4c and 5c for clarity since  $T_{actual} = 0$  when the particles have no relative motion – i.e., the particles have completely agglomerated. Two points are noteworthy when comparing these plots to their 3b, 4b, and 5b counterparts. First, the collapse when using  $T_{actual}$  is tighter since the actual (extracted)  $T$  values are used in the abscissa rather than a characteristic temperature ( $T_{est}$ ) estimated from input parameters. Second, as plotted in Figure 7 for systems with the same value of other dimensionless groups, i.e.,  $\phi = 0.05$ , the value of the transitional agglomerate number now overlaps for HCS and SSF.

Note that an *a priori* estimate and inclusion of the proportionality constant between  $T_{sys}$  and  $T_{actual}$  for each system would thus allow for a direct comparison of magnitudes of  $Ag$ , and thus an even more universal description of cohesive systems. Nonetheless, determining this constant of proportionality is non-trivial at best and beyond the scope of this work. Put another way,  $T_{actual}$  is an output (dependent variable), but regime maps are only useful in practice if the abscissa is a

function of inputs alone (independent variables). The implications of using the characteristic temperature  $T_{sys}$  rather than  $T_{actual}$  on the generality of regime maps is included in the Summary.

### 4.3 Collapse of enduring contact (dense) systems

Next we consider the behavior of denser systems in which enduring contacts dominate the behavior, to see if they collapse with  $Bo_G$  and/or  $Ag$ . In the dense PB system, collapse with  $Bo_G$  is observed for the porosity in both the experimental (Figure 8a) and simulated (Figure 8b) PB systems; similar plots are not shown for  $Ag$  since particles in the PB are static ( $T_{sys} = 0$ ) and thus  $Ag_{PB}$  is ill-defined. In Figure 8, a wide range of PB conditions were tested (8 experimental and 21 simulated). For the experimental PB, the source and magnitude of cohesion was varied by changing the humidity level of the fluidized air (van der Waals cohesion dominates at  $RH = 0\%$ , and capillary condensation becomes increasing important with increasing  $RH$ ). In simulations,  $F_{max}$  and  $x_{max}$  were varied for the square-force model. In both the experiments and simulations, different diameter particles were used, allowing for a larger range of  $Bo_{G,PB}$  to be tested. The list of conditions that PB experiments and simulations were performed is provided in Tables S9 and Table S10, respectively.

Additionally, the normalized discharge rates predicted in the hopper system collapse against  $Bo_{G,Hopper}$  but not  $Ag_{Hopper}$ , as evidenced in Figure 9. To achieve a range of different  $Bo_{G,Hopper}$  and  $Ag_{Hopper}$  values, simulations were carried out by varying  $A$  for the van der Waals cohesive source,  $RH$  for the condensed capillary cohesion source and  $F_{max}$  and  $x_{max}$  for the square-force cohesion source. Moreover, the particle density and Young's modulus were changed in order to further vary  $Bo_{G,Hopper}$  and  $Ag_{Hopper}$ . A full listing of the input parameters for the simulations is provided in Table S11 in the supplemental material.

Collectively, collapse of the dependent variable of interest against  $Bo_G$  but not  $Ag$  in these dense systems indicates that force is the appropriate micro-scale cohesive quantity for understanding the macro-scale behavior as opposed to energy. A plausible physical explanation is as follows: particles with enduring contacts need to overcome the maximum cohesive force, which occurs at contact (i.e., Fig. 1a), to induce relative (normal) motion; the concept of agglomeration vs. de-agglomeration (Fig. 1b) based on energy arguments is ill-defined in dense flows where contacts are enduring in nature.

#### 4.4 Revisiting Geldart's Chart

It is worth noting that the results described here may seem inconsistent with previous work on Geldart's chart<sup>18</sup> in which collapse with  $Bo_G$  (force-dominated) at the Group A/B border was found for a system that we report to collapse with  $Ag$  (energy-dominated) – namely, the bubbling bed experiments in Figure 6. For the case of van der Waals forces only, this collapse with  $Bo_G$  is fortuitous because an increase in  $F_{max}$  is linearly correlated to an increase in  $v_{crit}^2$  for van der Waals forces (numerators of  $Bo_G$  and  $Ag$ , respectively). In particular, consider a simple approximation of the  $F_{vdW}$  theory, i.e.,

$$F_{vdW} \approx Ar_s / (12x^2). \quad (22)$$

Using this approximation in conjunction with Eq. 1, the corresponding cohesive energy is obtained, namely  $W_{vdW} = -Ar_s / (12x)$ . Accordingly, from Eq. 2, an analytical expression for the critical agglomeration velocity can be found:

$$v_{crit,vdW}^2 \approx \frac{Ar_s}{6} \left( \frac{1}{x_{min}} - \frac{1}{x_{max}} \right) \frac{(1-e^2)}{me^2}. \quad (23)$$

From Eq. (22) and (23), it is seen that  $F_{vdW,max}$  ( $= F_{vdW}(x=x_{min})$ ) and  $v_{crit,vdW}^2$  are proportional to  $Ar_s$  and  $\frac{Ar_s}{m}$ , respectively, and thus the two numerators for  $Bo_G$  and  $Ag$ , namely  $F_{vdW,max}$  and  $KE_{crit,vdW}$

are proportional to one another – i.e.,  $F_{max} \propto KE_{crit} \propto Ar_s$ . Hence, a given system with van der Waals forces that collapses with  $Ag$  will also collapse with  $Bo_G$ , and vice versa (see Eq. 3 and 4). This provides an explanation as to why Geldart’s chart for fluidized bed (collision dominated), where van der Waals cohesion plays a role in the demarcation between groups C (cohesive), A (mildly-cohesive) and B (non-cohesive) collapses with  $Bo_G$ . Note in Figures 3 through 6, when looking at van der Waals forces only, collapse exists with  $Bo_G$  in addition to  $Ag$ , which is further support that  $F_{max}$  is proportional to  $KE_{crit}$  for van der Waals forces only.

#### **4.5 Changes in other dimensionless groups**

The (dimensionless) dependent variables of a system are a function of all relevant dimensionless groups for that system. Although the focus of the current work is on correctly identifying  $Ag$  or  $Bo_G$  as the appropriate dimensionless group that characterizes cohesion in a given system, there are other dimensionless groups that will impact the dependent variables – restitution coefficient  $e$ , etc. To demonstrate the robustness of the reported results, here we show that the collapse of  $Ag$  or  $Bo_G$  was also observed at different fixed values of other dimensionless groups that characterize the HCS system.

Figure 10 illustrates this robustness for HCS at a different solids volume fraction  $\phi$  (Figures 10a and 10b) and a different restitution coefficient  $e$  (Figures 10c and 10d). In Figure 10, the data markers are used to distinguish data from simulations with different fixed values of  $\phi$  and  $e$ . However, for the simulations with a given  $\phi$  and  $e$ , the denominators of  $Bo_{G,HCS}$  and  $Ag_{HCS}$  were varied by changing  $T_o$  and  $t$ , and the numerators were adjusted by using different sources of cohesion and different cohesion magnitudes (see supplemental material Table S6 for full listing). Collapse of  $N_{agg}/N_{tot}$  for different (fixed) values of  $\phi$  (Fig. 10a and 10b) and  $e$  (Fig. 10c and 10d) is not expected since  $\phi$  and  $e$  belong to the set of dimensionless groups (like  $Ag$  or  $Bo_G$ ) that

characterize the system. However, for any given fixed value of  $\phi$  and  $e$  (i.e., identical data markers),  $N_{agg}/N_{tot}$  collapses with  $Ag_{HCS}$  but not with  $Bo_{G,HCS}$ . Accordingly, the results presented above appear robust, as collapse is observed for  $Ag$  only for each constant pairing of  $e$  and  $\phi$  considered.

## 5. Concluding Remarks

### 5.1 Summary

A long-standing point of debate in cohesive-particle systems is whether a force-based or energy-based description of particle interactions is more appropriate. Estimates of agglomerate size,<sup>19,55-57</sup> constitutive relations for source terms in populations balances,<sup>24,58-63</sup> and regime maps<sup>15,26,62,64-69</sup> are a few prominent examples in which both force-based and energy-based descriptions have appeared in the literature, without justification as to why one is more appropriate than the other. Here we aim to decipher the force vs. energy conundrum.

We hypothesize that force-based considerations are more appropriate for enduring-contact (“dense”) systems and energy-based considerations are more appropriate for systems with brief contacts (“dilute”). The physical rationale is as follows: systems with sustained contacts (force chains) between particles must overcome a cohesive force to induce relative motion, so a force (momentum) balance is appropriate. Systems with brief (collisional) contacts must overcome energy losses associated with cohesion (in addition to non-cohesive losses like inelasticity) to avoid agglomeration, so an energy balance is appropriate. To test this hypothesis, experiments and simulations were performed for a wide range of systems (simple shear flow, homogeneous cooling, riser, bubbling fluidized bed, packed bed, and hopper flow) experiencing different types of cohesion (van der Waals, capillary bridges, and square-force); both material properties and system conditions were systematically varied. For a given system, the dimensionless, dependent variable



was plotted against two dimensionless numbers indicative of cohesion levels – a generalized Bond number  $Bo_G$ , which is the ratio of maximum cohesive force to the force driving flow, and a new Agglomerate number  $Ag$ , which is the ratio of critical cohesive energy for agglomeration to a characteristic granular energy for the system. The resulting plots showed collapse of the dense systems with  $Bo_G$  but not  $Ag$ , and vice versa for the dilute systems, thereby providing robust support for the hypothesis.

### **5.2 Implications: Regime Maps**

Regime maps for cohesive-particle flows have been a mainstay in industry for the prediction of various unit operations.<sup>1,13-15,26,62,64-70</sup> The generality (or lack thereof) of a given regime map depends on what quantities are being plotted. For example, Geldart's<sup>1</sup> chart is developed for fluidized beds at ambient conditions with van der Waals forces as the only possible source of cohesion. Application of Geldart's<sup>1</sup> chart to a fluidized bed operating at non-ambient temperatures or pressures, or application to a different apparatus (e.g., rotating tumbler) is not appropriate. Generally speaking, while system-specific nature of a regime map is difficult to overcome, its application to other material properties, operating conditions and/or sources of cohesion is possible via the use of appropriate dimensionless groups. Consider another well-known example – the laminar-to-turbulent transition in single-phase flow as characterized by the Reynolds number ( $Re$ ). The definition of the Reynolds number is broadly defined as the ratio of the inertial to viscous stresses in a fluid flow field or  $Re = \rho_f UL_{sys}/\mu$  (not system specific), but the explicit form of the Reynolds number is system specific as it depends on the length scale  $L_{sys}$  relevant to the particular system geometry, e.g., diameter  $D$  of a circular pipe ( $Re_{pipe} = \rho_f UD/\mu$ ), length along a flat plate  $L_p$  for boundary layer flow ( $Re_{plate} = \rho_f UL_p/\mu$ ), and particle diameter for flow of a spherical particle ( $Re_{particle} = \rho_f Ud/\mu$ ). For circular pipes, the critical value of  $Re$

demarcating laminar and turbulent flow regimes is  $Re_{crit,pipe} \sim 2100$ . Any changes to material properties, characteristic velocity or system dimensions are reflected in the value  $Re$  being compared to  $Re_{crit}$ , whereas the value of  $Re_{crit}$  itself (the regime map) only changes if the system geometry changes (circular pipe, square pipe, flow over flat plate, etc.). Similar to  $Re$ , our definitions of  $Bo_G$  (Eq. 3) and  $Ag$  (Eq. 4) are broadly defined for any system, and thus the explicit form for a specific system depends on input variables corresponding to the given system. Furthermore, it is worthwhile to note that  $Bo_G$  and  $Ag$  are just two of the dimensionless groups making up a full dimensionless set for a given system and that this full set is not unique; e.g., an equivalent set can be formed via multiplication of one dimensionless group by another, and replacement of the original group by said product.

The findings reported here are critical for building more universal regime maps – ones that are independent of cohesion source, as well as material properties and operating conditions. Our results indicate that two pertinent dimensionless groups for cohesion are  $Bo_G$  and  $Ag$ :  $Bo_G$  (force-based) is appropriate for systems with enduring collisions only (dense),  $Ag$  (energy-based) is appropriate for systems with brief collisions only (dilute), and both  $Bo_G$  and  $Ag$  would be needed for systems in which both types of contacts are present. There are likely numerous other dimensionless groups needed to fully characterize a given system (solids fraction, restitution coefficient, density ratio, etc.) which are not related to cohesion, and hence not the focus of this work. Similarly, unlike the monodisperse systems considered here, more complex systems would lead to even more dimensionless groups (size ratio, particle size distribution, etc.).

As alluded to above, future regime maps based on  $Bo_G$  and/or  $Ag$  will be system-dependent, similar to how the form and critical Reynolds number for the laminar-turbulent transition of single-phase flows depends on the specific geometry (circular pipe, square pipe, flow

over flat plate, etc.). However, when presented in dimensionless form, the regime maps will be applicable to different types of cohesion, materials, operating conditions. The applicability of a given  $Bo_G$ - and/or  $Ag$ -based regime map to different types of cohesion (van der Waals, capillary bridges, etc.) is a particularly novel aspect of this work representing a considerable step toward a more general description of cohesive systems.

### **5.3 Implications: Particle-level cohesion model and determination of $F_{max}$ and $v_{crit}^2$**

To construct regime maps, an estimate of  $F_{max}$  or  $v_{crit}^2$  is required for the numerators of  $Bo_G$  (Eq. 3) and  $Ag$  (Eq. 4), respectively. In this work, estimates for these quantities were based on complex, rigorous force models for van der Waals forces (Eq. 5) and humidity effects (Table 2). Such particle cohesion models can take years to develop and validate,<sup>21,35,39</sup> which leads to two practical questions: (i) what is the minimal yet sufficient physics needed in such a model? (ii) can the corresponding model parameters be extracted from a simple bulk experiment?

Regarding (i), the results obtained here suggest that the simplest form of a particle cohesion model should be one which maintains the characteristic force ( $F_{max}$ ) and energy ( $mv_{crit}^2$ ) of cohesion, as all of the systems considered here collapsed with  $Bo_G$  or  $Ag$ . Such a “square-force” model – one in which a constant force occurs at small separation distances and then drops to zero at a specified cutoff distance (Eq. 10) – was proposed recently by Liu et al.<sup>30</sup> In their work, the constant force in the square-force model was set equal to  $F_{max}$  of more rigorous models, and the cutoff distance was chosen such that area under the curve equals the critical cohesion energy, or  $mv_{crit}^2$ , of the more rigorous models. DEM simulations of both dilute and dense many-particle systems showed that the resulting square-force model compares well with more rigorous forms of cohesion models, thereby providing initial validation for the square-force approach.<sup>30</sup>

Regarding (ii), the parameters for this simplified, square-force model of particle cohesion can be extracted in straightforward manner for lightly cohesive particles, as described recently by Liu et al.<sup>30</sup> In particular, the defluidization curve of a fluidized bed (pressure drop vs. gas velocity) was used in conjunction with DEM simulations to determine  $F_{max}$  and the cutoff distance (and hence  $v_{crit}$ ) in a sequential manner designed to isolate their effects. Extension to more cohesive particles is currently underway via the use of a commercial rheometer.<sup>71</sup> Such straightforward bulk experiments that can be used to extract the parameters of the square-force model represent a much-needed alternative to the protracted development of more rigorous, and unnecessarily complex, cohesion models.

#### ***5.4 Implications: DEM simulations***

As described above, the square-force model captures all that is needed in a simplified model of cohesion, namely the characteristic force and energy, to correctly predict interactions among cohesive particles. Although a more rigorous description (e.g., Eq. 5 for van der Waals forces) is capable of providing a more accurate force vs. separation distance curve, the results obtained here and prior results<sup>30</sup> indicate that such complexity is not required for purposes of DEM simulations.

#### ***5.5 Implications: Continuum theory***

The results obtained here provide an answer to the longstanding question as to whether force-based<sup>56,72</sup> or energy-based<sup>24,58,59</sup> closures to population balances are more appropriate. Specifically, a continuum theory capable of predicting the behavior of cohesive particles requires consideration of  $F_{max}$  (force) for dense systems and  $v_{crit}^2$  (energy) for dilute flows, or both for flows with both enduring and short (nearly-instantaneous) contacts. The two concentration limits can be

unified via the radial distribution function  $g_o(\phi, x)$  – i.e.,  $\lim_{\phi \rightarrow \phi_{max}} \frac{\int_0^{x_{max}} F_c(x) g_o(\phi, x) dx}{\int_0^{x_{max}} g_o(\phi, x) dx} = F_{max}$  in

the limit of dense flows, and  $\lim_{\phi \rightarrow 0} \frac{\int_0^{x_{max}} F_c(x) g_o(\phi, x) dx}{\int_0^{x_{max}} g_o(\phi, x) dx} = \frac{W}{x_{max}}$  for dilute.

### **Acknowledgements**

The authors are grateful to Dow Corning Corporation for providing the funding for this work. This work utilized the RMACC Summit supercomputer, which is supported by the National Science Foundation (awards ACI-1532235 and ACI-1532236), the University of Colorado Boulder, and Colorado State University. The Summit supercomputer is a joint effort of the University of Colorado Boulder and Colorado State University. Additionally, the authors would like to thank Andrew Miller, Kacey Paulin and Haley Manchester for their efforts conducting experiments.

## References

1. Geldart D. Types of gas fluidization. *Powder Technol.* 1973;7(5):285-292.
2. Blum J. Laboratory Experiments on Preplanetary Dust Aggregation. *Space Sci Rev.* 2000;92(1):265-278.
3. Rozitis B, MacLennan E, Emery JP. Cohesive forces prevent the rotational breakup of rubble-pile asteroid (29075) 1950 DA. *Nature.* 2014;512(7513):174-176.
4. Shi D, Abatan AA, Vargas WL, McCarthy JJ. Eliminating Segregation in Free-Surface Flows of Particles. *Phys Rev Lett.* 2007;99(14):148001.
5. Zhang P, Law CK. An analysis of head-on droplet collision with large deformation in gaseous medium. *Phys Fluids.* 2011;23(4):042102.
6. Veen SJ, Antoniuk O, Weber B, et al. Colloidal Aggregation in Microgravity by Critical Casimir Forces. *Phys Rev Lett.* 2012;109:248302.
7. Urvoy A, Ripka F, Lesanovsky I, et al. Strongly Correlated Growth of Rydberg Aggregates in a Vapor Cell. *Phys Rev Lett.* 2015;114(20):203002.
8. Chew JW, Cahyadi A, Hrenya CM, Karri R, Cocco RA. Review of entrainment correlations in gas-solid fluidization. *Chem Eng J.* 2015;260(C):152-171.
9. Cahyadi A, Neumayer AH, Hrenya CM, Cocco RA, Chew JW. Comparative study of Transport Disengaging Height (TDH) correlations in gas-solid fluidization. *Powder Technol.* 2015;275:220-238.
10. Shabaniyan J, Jafari R, Chaouki J. Fluidization of ultrafine powders. *Int Rev Chem Eng.* 2012;4(1):16-50.
11. Valverde JM, Castellanos A. Types of gas fluidization of cohesive granular materials. *Phys Rev E.* 2007;75(3):031306.
12. Castellanos A, Valverde JM, Quintanilla MAS. Physics of Compaction of Fine Cohesive Particles. *Phys Rev Lett.* 2005;94(7):075501.

13. Li H, McCarthy JJ. Phase diagrams for cohesive particle mixing and segregation. *Phys Rev E*. 2005;71:021305.
14. Jain K, Shi D, McCarthy JJ. Discrete characterization of cohesion in gas–solid flows. *Powder Technol*. 2004;146(1-2):160-167.
15. Nase ST, Vargas WL, Abatan AA, McCarthy JJ. Discrete characterization tools for cohesive granular material. *Powder Technol*. 2001;116(2-3):214-223.
16. Trappe V, Prasad V, Cipelletti L, Segre PN, Weitz DA. Jamming phase diagram for attractive particles. *Nature*. 2001;411(6839):772-775.
17. Web of Science, Accessed Feb. 8, 2020.
18. Molerus O. Interpretation of Geldart's type A, B, C and D powders by taking into account interparticle cohesion forces. *Powder Technol*. 1982;33(1):81-87.
19. Forsyth AJ, Hutton SR, Osborne CF, Rhodes MJ. Effects of Interparticle Force on the Packing of Spherical Granular Material. *Phys Rev Lett*. 2001;87(24):244301.
20. Forsyth AJ, Hutton SR, Rhodes MJ, Osborne CF. Effect of applied interparticle force on the static and dynamic angles of repose of spherical granular material. *Phys Rev E*. 2001;63(3):031302.
21. LaMarche CQ, Miller AW, Liu P, Hrenya CM. Linking micro-scale predictions of capillary forces to macro-scale fluidization experiments in humid environments. *AIChE J*. 2016;62(10):3585-3597.
22. Dahneke B. The capture of aerosol particles by surfaces. *J Colloid Interface Sci*. 1971;37(2):342-353.
23. Castellanos A, Valverde JM, Quintanilla MAS. Aggregation and sedimentation in gas-fluidized beds of cohesive powders. *Phys Rev E*. 2001;64(4):041304.
24. Kantak AA, Hrenya CM, Davis RH. Initial rates of aggregation for dilute, granular flows of wet particles. *Phys Fluids*. 2009;21(2):023301.

25. Shabanian J, Duchesne MA, Runstedtler A, Syamlal M, Hughes RW. Improved analytical energy balance model for evaluating agglomeration from a binary collision of identical wet particles. *Chem Eng Sci.* 2020;223.
26. Strauch S, Herminghaus S. Wet granular matter: a truly complex fluid. *Soft Matter.* 2012;8(32):8271-8280.
27. Israelachvili JN. *Intermolecular and surface forces* (3rd edition). Boston: Academic Press; 2011.
28. Seville JPK, Tüzün U, Clift R. *Processing of Particulate Solids*. New York: Chapman & Hall; 1997.
29. Fingerle A, Roeller K, Huang K, Herminghaus S. Phase transitions far from equilibrium in wet granular matter. *New J Phys.* 2008;10(5):053020.
30. Liu P, LaMarche CQ, Kellogg KM, Hrenya CM. A square-force cohesion model and its extraction from bulk measurements. *AIChE J.* 2018;64(7):2329-2339.
31. Foerster SF, Louge MY, Chang H, Allia Kd. Measurements of the collision properties of small spheres. *Phys Fluids.* 1994;6(3):1108-1115.
32. Kobayashi T, Tanaka T, Shimada N, Kawaguchi T. DEM–CFD analysis of fluidization behavior of Geldart Group A particles using a dynamic adhesion force model. *Powder Technol.* 2013;248:143-152.
33. Gu Y, Ozel A, Sundaresan S. A modified cohesion model for CFD–DEM simulations of fluidization. *Powder Technol.* 2016;296:17-28.
34. Liu P, LaMarche CQ, Kellogg KM, Hrenya CM. Fine-particle defluidization: Interaction between cohesion, Young’s modulus and static bed height. *Chem Eng Sci.* 2016;145:266-278.
35. LaMarche CQ, Leadley S, Liu P, Kellogg KM, Hrenya CM. Method of quantifying surface roughness for accurate adhesive force predictions. *Chem Eng Sci.* 2017;158:140-153.
36. Liu P, LaMarche CQ, Kellogg KM, Leadley S, Hrenya CM. Cohesive grains: Bridging microlevel measurements to macrolevel flow behavior via surface roughness. *AIChE J.* 2016;62(10):3529-3537.



37. Rabinovich YI, Adler JJ, Ata A, Singh RK, Moudgil BM. Adhesion between nanoscale rough surfaces I. role of asperity geometry. *J Colloid Interface Sci.* 2000;232(1):10-16.
38. Rabinovich YI, Adler JJ, Ata A, Singh RK, Moudgil BM. Adhesion between nanoscale rough surfaces II. measurement and comparison with theory. *J Colloid Interface Sci.* 2000;232(1):17-24.
39. LaMarche CQ, Miller AW, Liu P, Leadley S, Hrenya CM. How nano-scale roughness impacts the flow of grains influenced by capillary cohesion. *AIChE J.* 2017;63(12):5250-5257.
40. Orr FM, Scriven LE, Rivas AP. Pendular rings between solids: meniscus properties and capillary force. *J Fluid Mech.* 1975;67(4):723-742.
41. Butt H-J, Graf K, Kappl M. *Physics and Chemistry of Interfaces.* 1 ed: Wiley-VCH; 2003.
42. Pierrat P, Caram HS. Tensile strength of wet granular materials. *Powder Technol.* 1997;91:83-93.
43. Xiao X, Qian L. Investigation of Humidity-Dependent Capillary Force. *Langmuir.* 2000;16(21):8153-8158.
44. Butt H-J, Kappl M. Normal capillary forces. *Adv Colloid Interface Sci.* 2009;146(1-2):48-60.
45. Weber MW, Hoffman DK, Hrenya CM. Discrete-particle simulations of cohesive granular flow using a square-well potential. *Granular Matter.* 2004;6(4):239-254.
46. Campbell CS. Stress tensor for Simple shear flows of a granular material *J Fluid Mech.* 1989;203:449-473.
47. Bagnold RA. Experiments on a gravity-free dispersion of large solid spheres in a Newtonian fluid under shear. *Proc R Soc London, Ser A.* 1954.
48. Fullmer WD, Hrenya CM. The Clustering Instability in Rapid Granular and Gas-Solid Flows. *Annu Rev Fluid Mech.* 2017;49(1):485-510.
49. Haff PK. Grain flow as a fluid-mechanical phenomenon. *J Fluid Mech.* 1983;134:401-430.
50. Garzó V. Instabilities in a free granular fluid described by the Enskog equation. *Phys Rev E.* 2005;72(2):021106.

51. Rhodes M. *Introduction to Particle Technology (2nd edition)*. Chichester: John Wiley & Sons; 2008.
52. Garzó V, Tenneti S, Subramaniam S, Hrenya CM. Enskog kinetic theory for monodisperse gas–solid flows. *J Fluid Mech.* 2012;712:129-168.
53. LaMarche CQ, Liu P, Kellogg KM, Hrenya CM. Fluidized-bed measurements of carefully-characterized, mildly-cohesive (Group A) particles. *Chem Eng J.* 2017;310, Part 1:259-271.
54. Tsinontides SC, Jackson R. The mechanics of gas fluidized beds with an interval of stable fluidization. *J Fluid Mech.* 1993;255:237-274.
55. van Wachem B, Sasic S. Derivation, simulation and validation of a cohesive particle flow CFD model. *AIChE J.* 2008;54(1):9-19.
56. Motlagh AHA, Grace JR, Salcudean M, Hrenya CM. New structure-based model for Eulerian simulation of hydrodynamics in gas–solid fluidized beds of Geldart group “A” particles. *Chem Eng Sci.* 2014;120:22-36.
57. Zhou T, Li H, Shinohara K. Agglomerating fluidization of group C particles: major factors of coalescence and breakup of agglomerates. *Adv Powder Technol.* 2006;17(2):159-166.
58. Liu L. Kinetic theory of aggregation in granular flow. *AIChE J.* 2011;57(12):3331-3343.
59. Kellogg KM, Liu P, LaMarche CQ, Hrenya CM. Continuum theory for rapid cohesive-particle flows: general balance equations and discrete-element-method-based closure of cohesion-specific quantities. *J Fluid Mech.* 2017;832:345-382.
60. Sun L, Luo K, Fan J. Population Balance Equation of Cohesive Particle Flow in a Circulating Fluidized Bed. *Chem Eng Technol.* 2017;40(9):1544-1551.
61. Sun L, Yu W, Hassan M, Wang S, Liu G, Lu H. Investigation of Aggregation Kernel and Simulation of Cohesive Particle Flow. *Chem Eng Technol.* 2016;39(10):1858-1866.
62. Castellanos A, Valverde JM, Pérez AT, Ramos A, Watson PK. Flow regimes in fine cohesive powders. *Phys Rev Lett.* 1999;82(6):1156.

63. Narni NR, Peglow M, Warnecke G, Kumar J, Heinrich S, Kuipers JAM. Modeling of aggregation kernels for fluidized beds using discrete particle model simulations. *Particuology*. 2014;13(Supplement C):134-144.
64. Liu D, van Wachem BGM, Mudde RF, Chen X, van Ommen JR. An adhesive CFD-DEM model for simulating nanoparticle agglomerate fluidization. *AIChE J*. 2016;62(7):2259-2270.
65. Shi H, Roy S, Weinhart T, Magnanimo V, Luding S. Steady state rheology of homogeneous and inhomogeneous cohesive granular materials. *Granular Matter*. 2019;22(1).
66. Gonzalez S, Thornton AR, Luding S. Free cooling phase-diagram of hard-spheres with short- and long-range interactions. *Eur Phys J Spec Top*. 2014;223(11):2205-2225.
67. Jarray A, Shi H, Scheper BJ, Habibi M, Luding S. Cohesion-driven mixing and segregation of dry granular media. *Sci Rep*. 2019;9(1):13480.
68. Girardi M, Radl S, Sundaresan S. Simulating wet gas–solid fluidized beds using coarse-grid CFD-DEM. *Chem Eng Sci*. 2016;144:224-238.
69. van Wachem B, Thalberg K, Nguyen D, Martin de Juan L, Remmelgas J, Niklasson-Bjorn I. Analysis, modelling and simulation of the fragmentation of agglomerates. *Chem Eng Sci*. 2020;227.
70. Pohl S, Kleinebudde P. A review of regime maps for granulation. *Int J Pharm*. 2020;587:119660.
71. Mishra I, Liu P, Shetty A, Hrenya CM. On the use of a powder rheometer to probe defluidization of cohesive particles. *Chem Eng Sci*. 2020;214.
72. van Wachem B, Sasic S. Derivation, simulation and validation of a cohesive particle flow CFD model. *AIChE J*. 2008;54(1):9-19.

List of Table captions

**Table 1.** Overview of the systems considered.

**Table 2.** Equations for solving the condensed capillary force.

## List of Figure captions

**Figure 1.** Force (a) and kinetic energy (b) profiles for the approach, collision, and rebound of two cohesive particles. (a) The cohesive force  $F_c$  depends only on separation distance  $x$  so no hysteresis occurs. (b) Dissipation of  $KE$  during collision of particles leads to hysteresis. Dashed and solid lines illustrate two scenarios that depend on initial  $KE$  and/or level of dissipation during the collision. The dashed lines represent particle pair  $a$  that have a high enough initial  $KE$  ( $0.5v_{i,a}^2 > 0.5v_{crit}^2$ ) to fully separate (no agglomerate forms). The solid lines represent particle pair  $b$  that do not have a high enough initial  $KE$  ( $0.5v_{i,b}^2 \leq 0.5v_{crit}^2$ ) to avoid agglomeration.

**Figure 2.** The source of  $T_{sys}$  identified in each system (plotted on  $x$ -axis) is proportional to the measured value  $T_{actual}$  (plotted on  $y$ -axis) for (a) SSF and (b) HCS.

**Figure 3.** SSF simulation: Fraction of particles in agglomerates plotted against (a)  $BO_{G,SSF}$  and (b)  $Ag_{SSF}$ . (c) Fraction of particles in agglomerates plotted against  $1/Ag$  determined using the measured (output)  $T_{actual}$ . The shape and color of the marker indicates the source of cohesion, i.e., square-force model (black circle), van der Waals (yellow star), and relative humidity (red square). Along a given line connecting the same type of markers, only the shear rate  $\gamma$  is changed. Different lines denote a given cohesion source (same line type), and are obtained by varying the cohesion magnitude ( $A$  for  $F_{vdW}$ ,  $RH$  for  $F_{RH}$ , and  $F_{max}$  and  $x_{max}$  for  $F_{sf}$ ) and particle properties ( $E$  and  $d$ ). Collectively, results from 63 simulations are plotted; see supplementary Table S5 for listing of inputs. Dimensionless groups  $\phi = 0.05$ ,  $e = 0.97$ , and  $L/d = 13.78$  were kept constant.

**Figure 4.** HCS simulation: Fraction of particles in agglomerates from the simulated HCS plotted against (a)  $BO_{G,HCS}$  and (b)  $Ag_{HCS}$ . (c) Fraction of particles in agglomerates plotted against  $1/Ag$  determined using the measured (output)  $T_{actual}$ . The shape and color of the marker indicates the source of cohesion, i.e., square-force model (black circle), van der Waals (yellow star), and relative humidity (red square), and lines only connect data points for the time evolution of HCS simulations with the same particle properties and  $T_o$ . The cohesion source input parameters  $A$ ,  $RH$ , and  $F_{max}$  and  $x_{max}$  were varied to adjust the cohesion magnitude (i.e.,  $F_{max}$  and  $v_{crit}^2$ ) for the van der Waals, condensed-capillary and square-force cohesion sources, respectively. Different lines denote a

given cohesion source and  $T_o$ , and were achieved by changing the particle diameter and Young's modulus. Results from HCS simulations run with 18 different conditions are plotted and the full list of conditions are tabulated in the supplemental material Table S6. Dimensionless groups  $\phi = 0.05$ ,  $e = 0.97$ , and  $L/d = 13.78$  were kept constant.

**Figure 5.** Riser simulation: Fraction of particles in agglomerates from the simulated riser plotted against (a)  $Bo_{G,Riser}$  and (b)  $Ag_{Riser}$ . (c) Fraction of particles in agglomerates plotted against  $1/Ag$ , which is determined from the measured (output) granular temperature  $T_{actual}$ . The shape and color of the marker indicates the source of cohesion, i.e., square-force model (black circle), van der Waals (yellow star), and relative humidity (red square). Different riser simulations for the same cohesion source (same marker type) are obtained by varying the cohesion magnitude ( $A$  for  $F_{vdW}$ ,  $RH$  for  $F_{RH}$ , and  $F_{max}$  and  $x_{max}$  for  $F_{sf}$ ), and the particle properties ( $E$ , and  $\rho_p$ ) and gas properties ( $\mu$  and superficial gas velocity). Results from riser simulations run with 36 different conditions are plotted, the conditions for which are provided in a table in the supplemental material Table S7. Dimensionless groups  $\phi = 0.01$ ,  $e = 0.97$ , and  $L/d = 50.5$  were kept constant.

**Figure 6.** BB experiments:  $U_{mb}$  measured from BB experiments plotted against (a)  $Bo_{G,BB}$  and (b)  $Ag_{BB}$ . The color and shape of the marker indicates the source of cohesion, van der Waals (yellow star), and relative humidity (red square), but each data point corresponds to a different set of experimental conditions (e.g., different particle diameter or relative humidity). Measurements with the same cohesion source (same marker type) are obtained by varying the cohesion magnitude ( $RH$  for  $F_{RH}$ ) and particle diameter ( $d$ ). A detailed list of the experimental conditions associated with the results are listed in a detailed table in the supplemental material (Table S8). Results are plotted from BB experiments run under 11 different conditions.

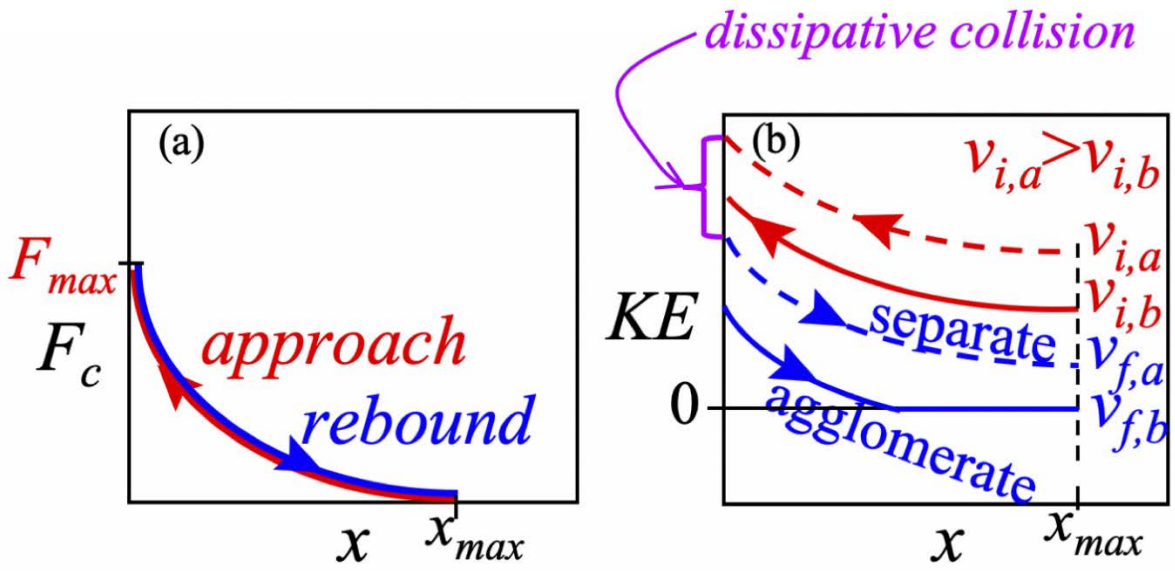
**Figure 7.** HCS and SSF simulations: fraction of particles in agglomerates plotted against  $1/Ag$ , which is determined using the actual (measured) granular temperature  $T_{actual}$ . The color and shape of the data markers indicates the system, i.e., HCS (black squares) or SSF (green circles). Lines only connect data points for the time evolution of HCS transient simulations with the same particle properties and  $T_o$ . The simulation results are originally plotted in Figures 3 and 4 and hence the

collapse of  $1/Ag$  for two systems is found for a wide range of simulation input conditions. Dimensionless groups  $\phi = 0.05$ ,  $e = 0.97$ , and  $L/d = 13.78$  for both the HCS and SSF were kept constant.

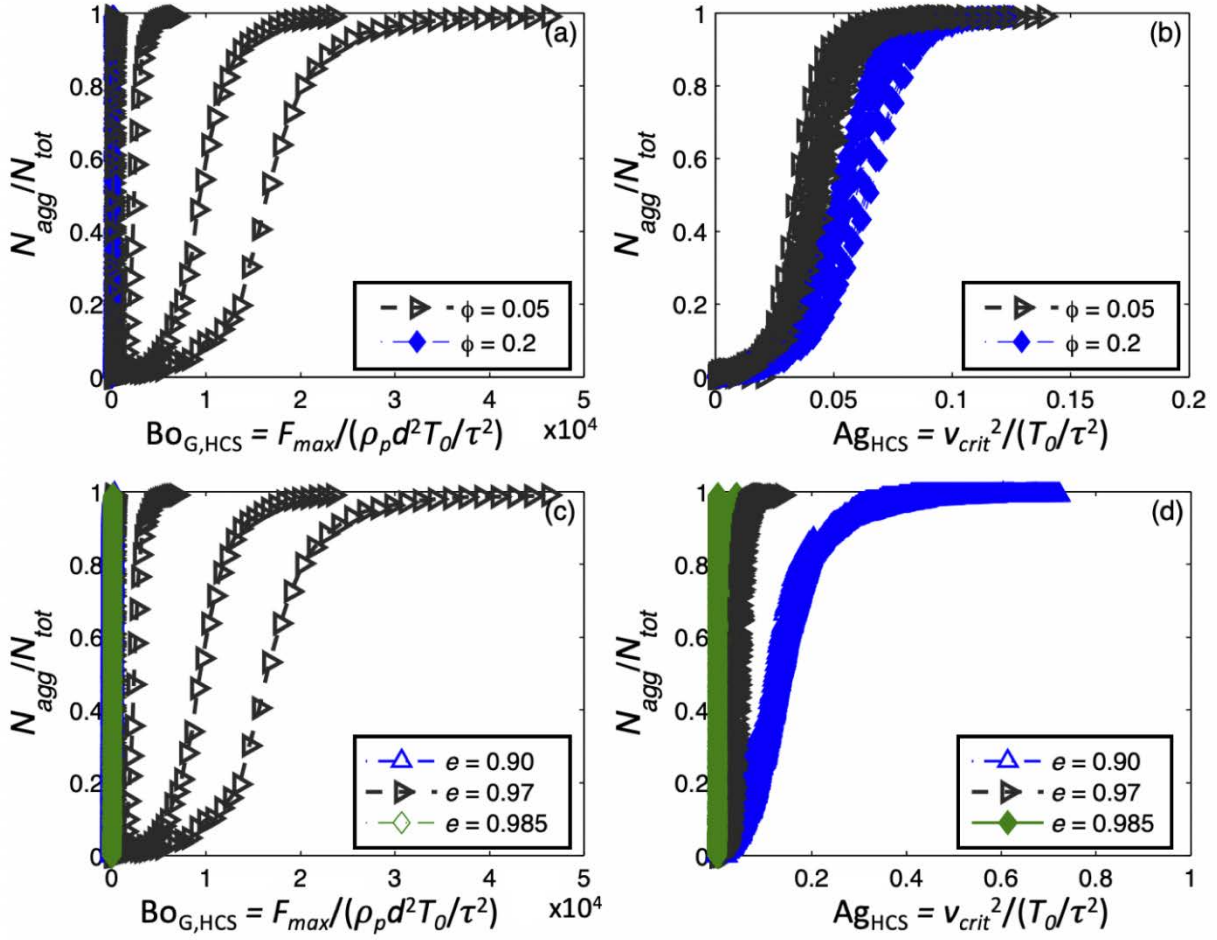
**Figure 8.** PB experiment and simulations: Porosity plotted against  $Bo_{G,PB}$  for the (a) experimental and (b) simulated systems. The color and shape of the marker indicates the source of cohesion, namely, van der Waals (yellow star), relative humidity (red square), and square-force cohesion (black circles). Each data point corresponds to a different set of conditions that are listed in detail in Table S9 (experiment) and Table S10 (DEM) in the supplemental material. Results from 8 different PB experimental conditions are plotted in (a) and 21 different PB simulations in (b).

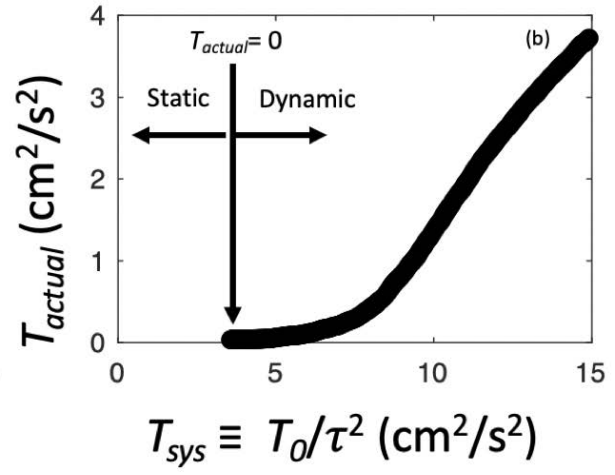
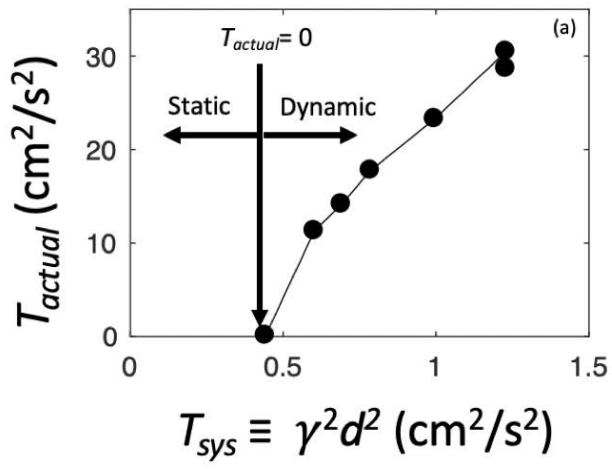
**Figure 9.** Hopper simulations: Normalized discharge rate of particles from the simulated hopper plotted against (a)  $Bo_{G,Hopper}$  and (b)  $Ag_{Hopper}$ . The color and shape of the marker indicates the source of cohesion, i.e., square-force model (black circle), van der Waals (yellow star), and relative humidity (red square), where each data point corresponds to a different set of hopper conditions that are listed in a detailed table in the supplemental material Table S11. Each data point corresponds to a different set of conditions (e.g., different Young's modulus, or particle density). Results from hopper simulations run with 21 different conditions are plotted.

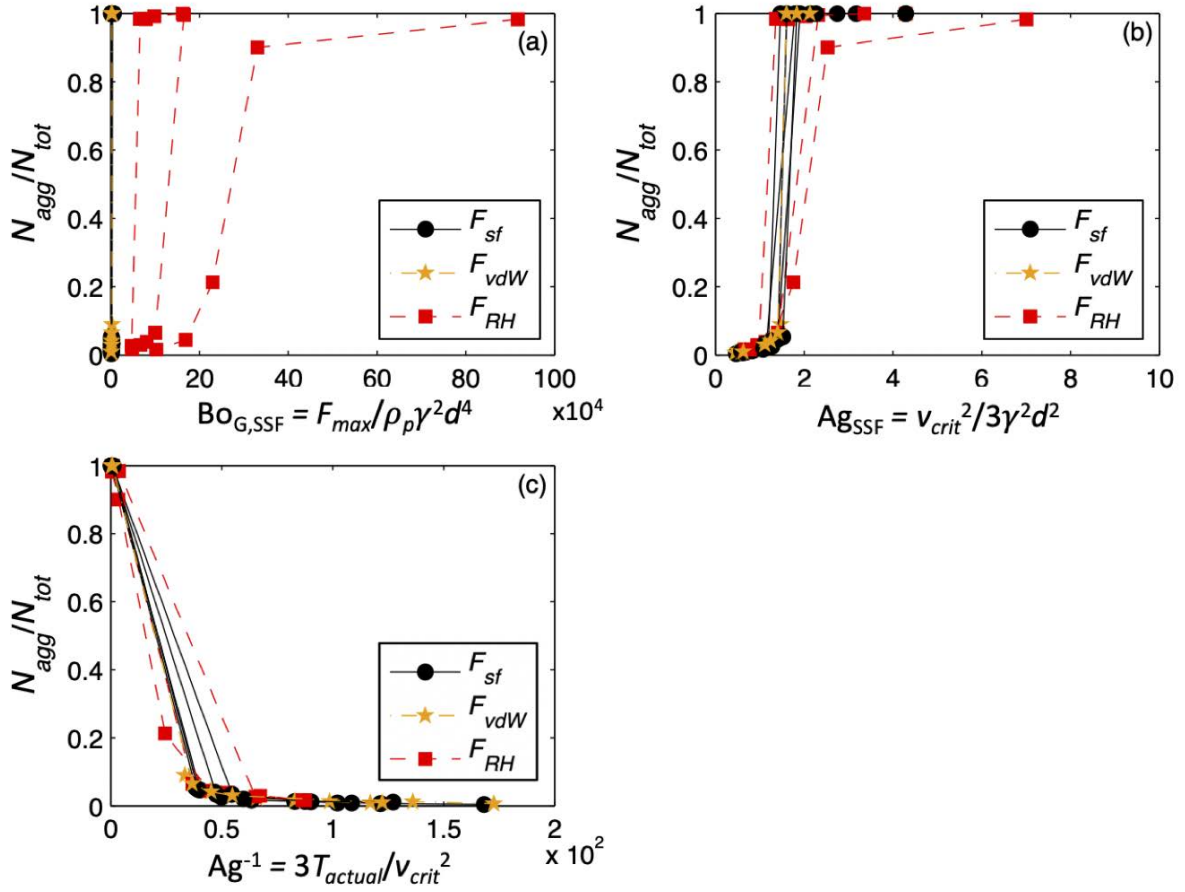
**Figure 10.** HCS simulations: fraction of particles in agglomerates for different solids volume fractions (dimensionless group) values of  $\phi = 0.05$  (black) and  $\phi = 0.2$  (blue) for increasing (a)  $Bo_{G,HCS}$  and (b)  $Ag_{HCS}$  ( $e = 0.97$ ); fraction of particles in agglomerates for different coefficient of restitution (dimensionless group) values of  $e = 0.90$  (blue),  $e = 0.97$  (black) and  $e = 0.985$  (green), on the fraction of particles in agglomerates with increasing (c)  $Bo_{G,HCS}$  and (d)  $Ag_{HCS}$  ( $\phi = 0.05$ ). Dimensionless groups  $e = 0.97$ , and  $L/d = 13.78$  were kept constant in (a) and (b). In (c) and (d), the dimensionless groups  $\phi = 0.05$ , and  $L/d = 13.78$  were kept constant.

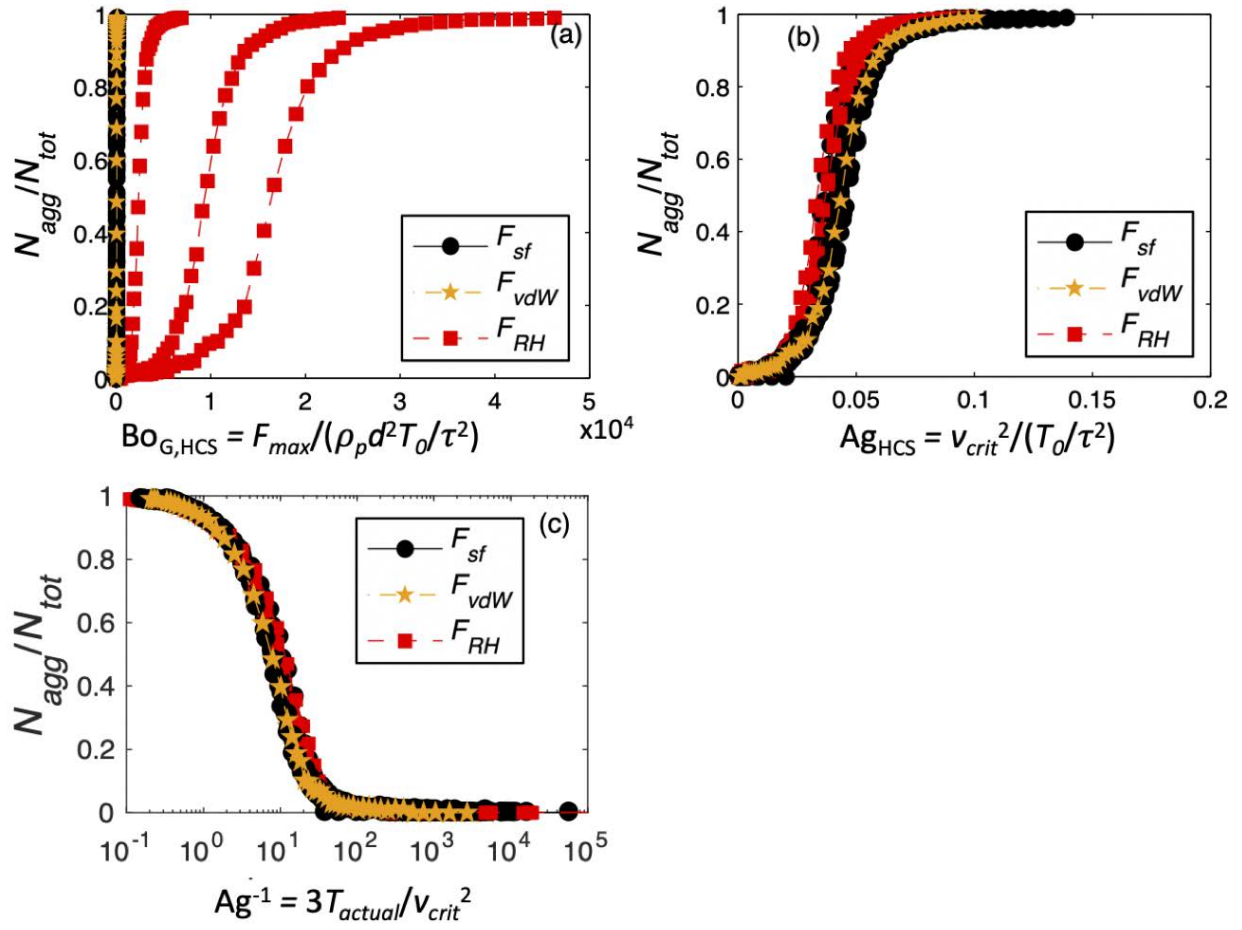


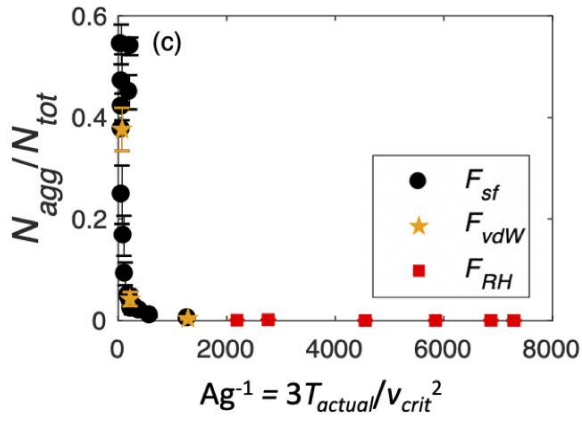
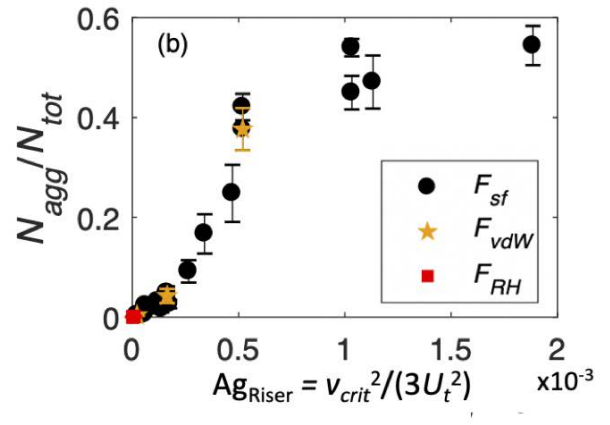
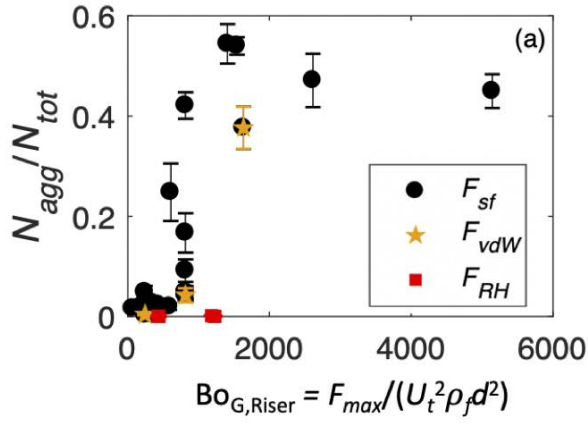


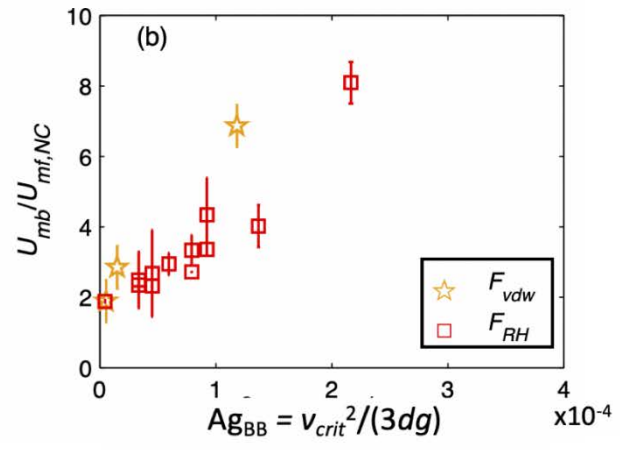
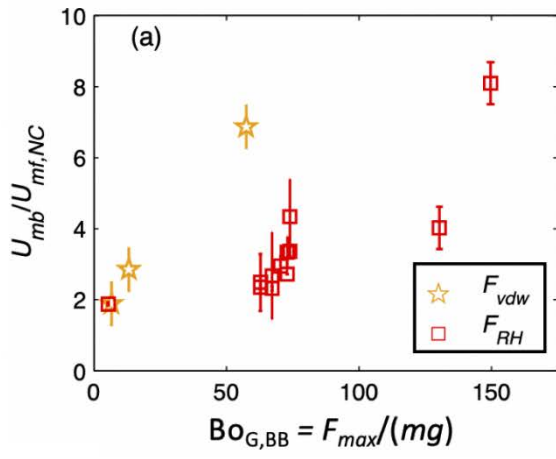


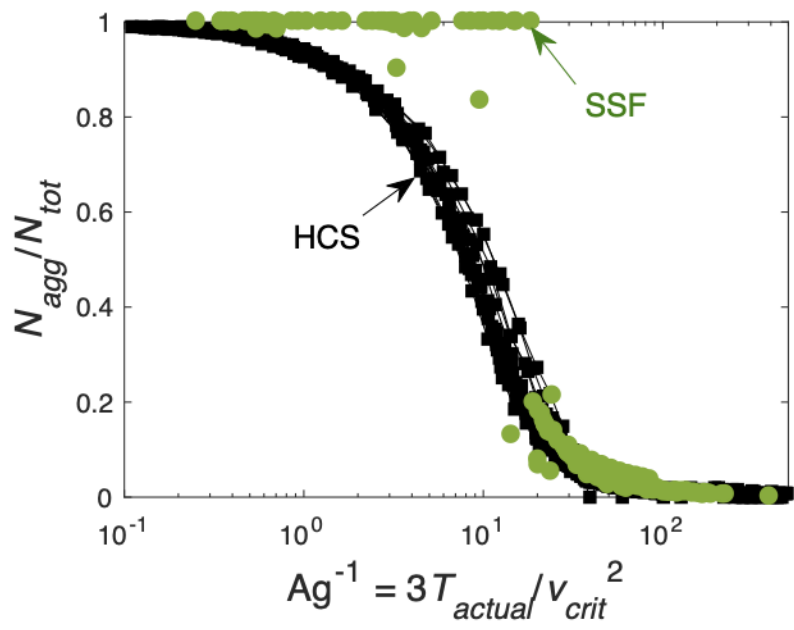


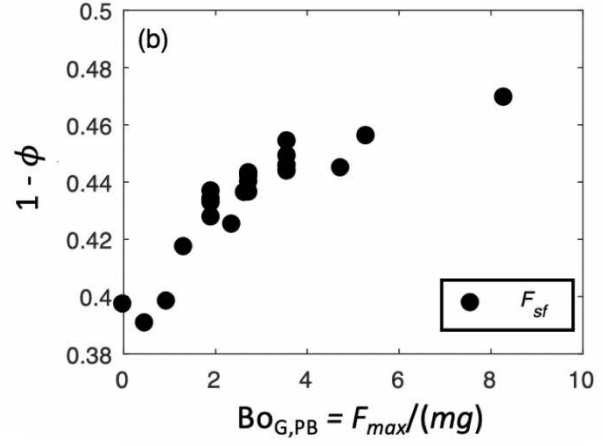
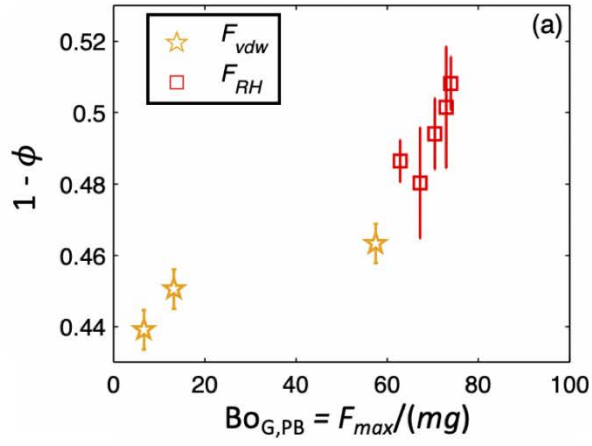




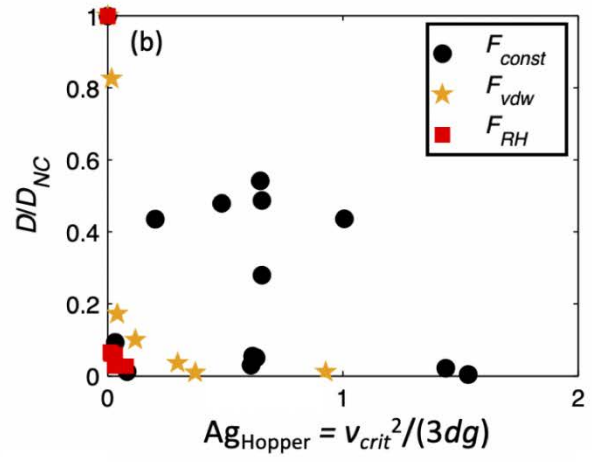
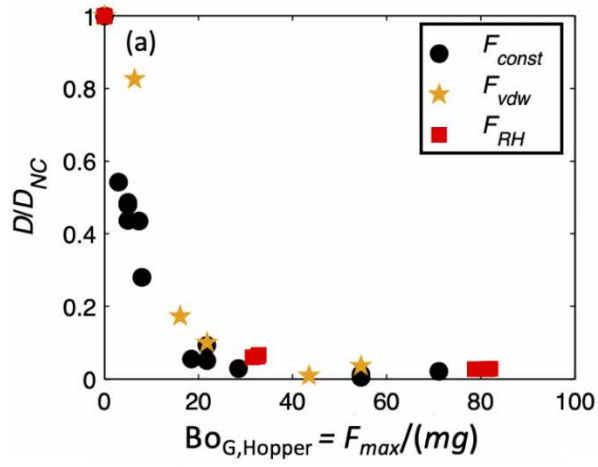


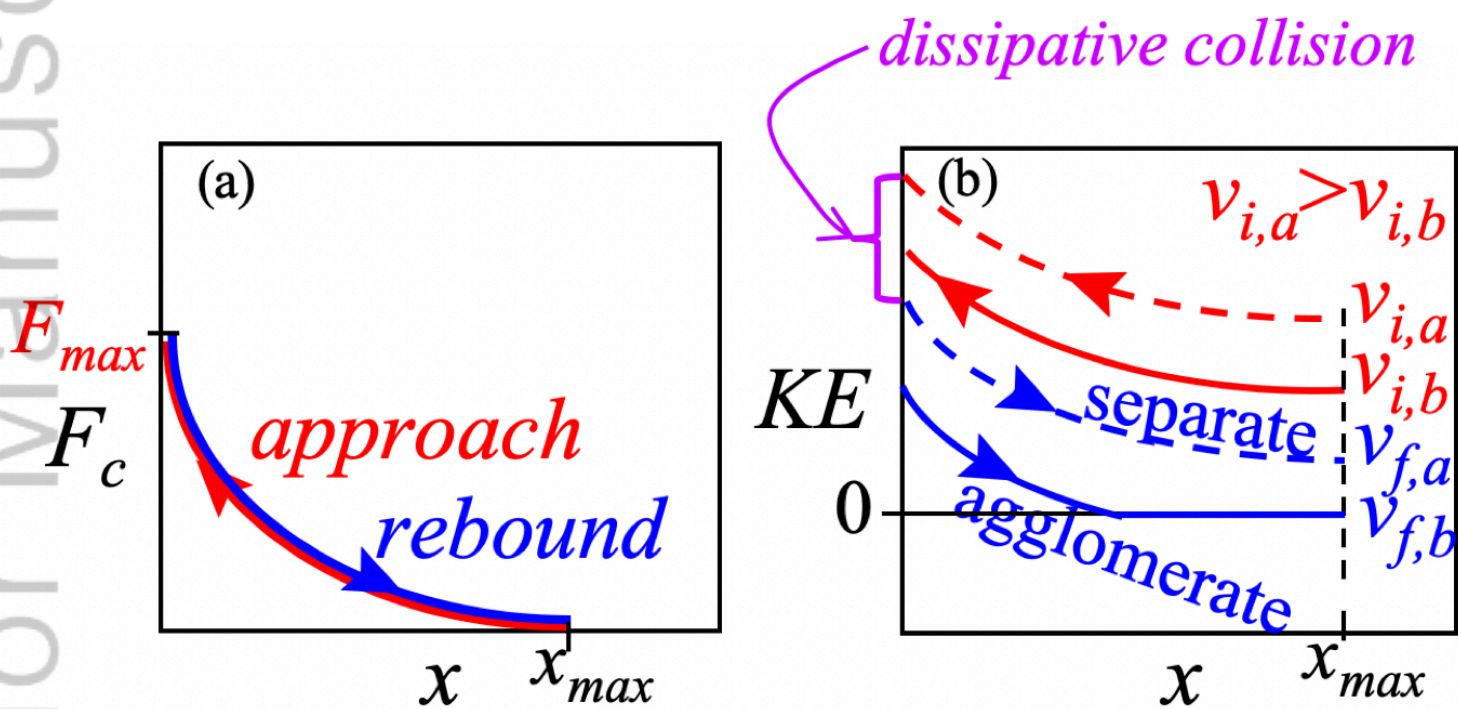




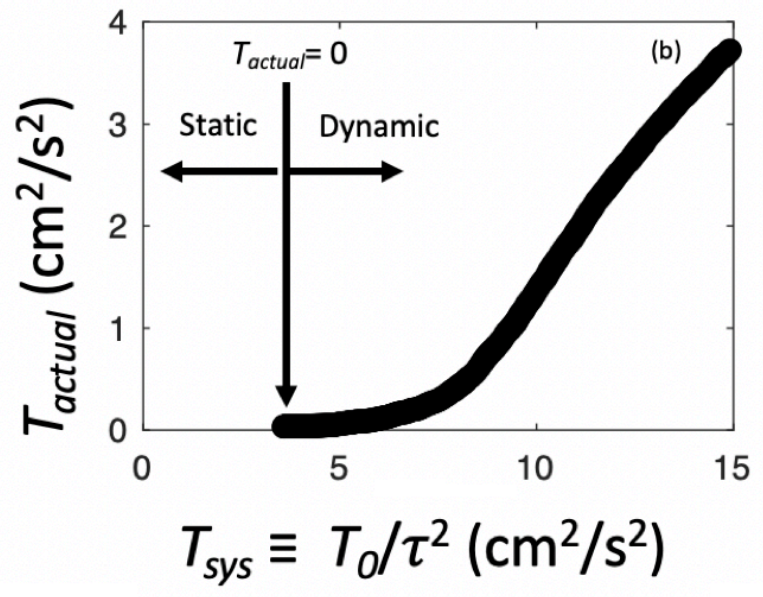
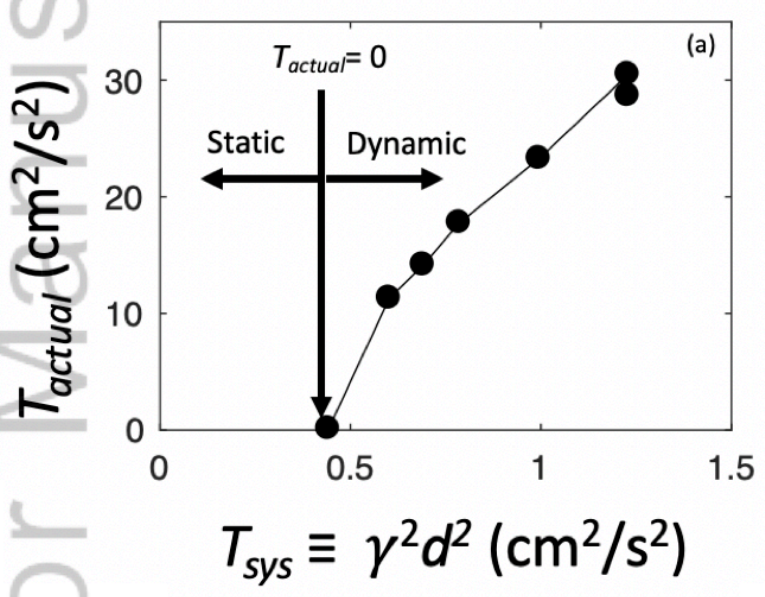




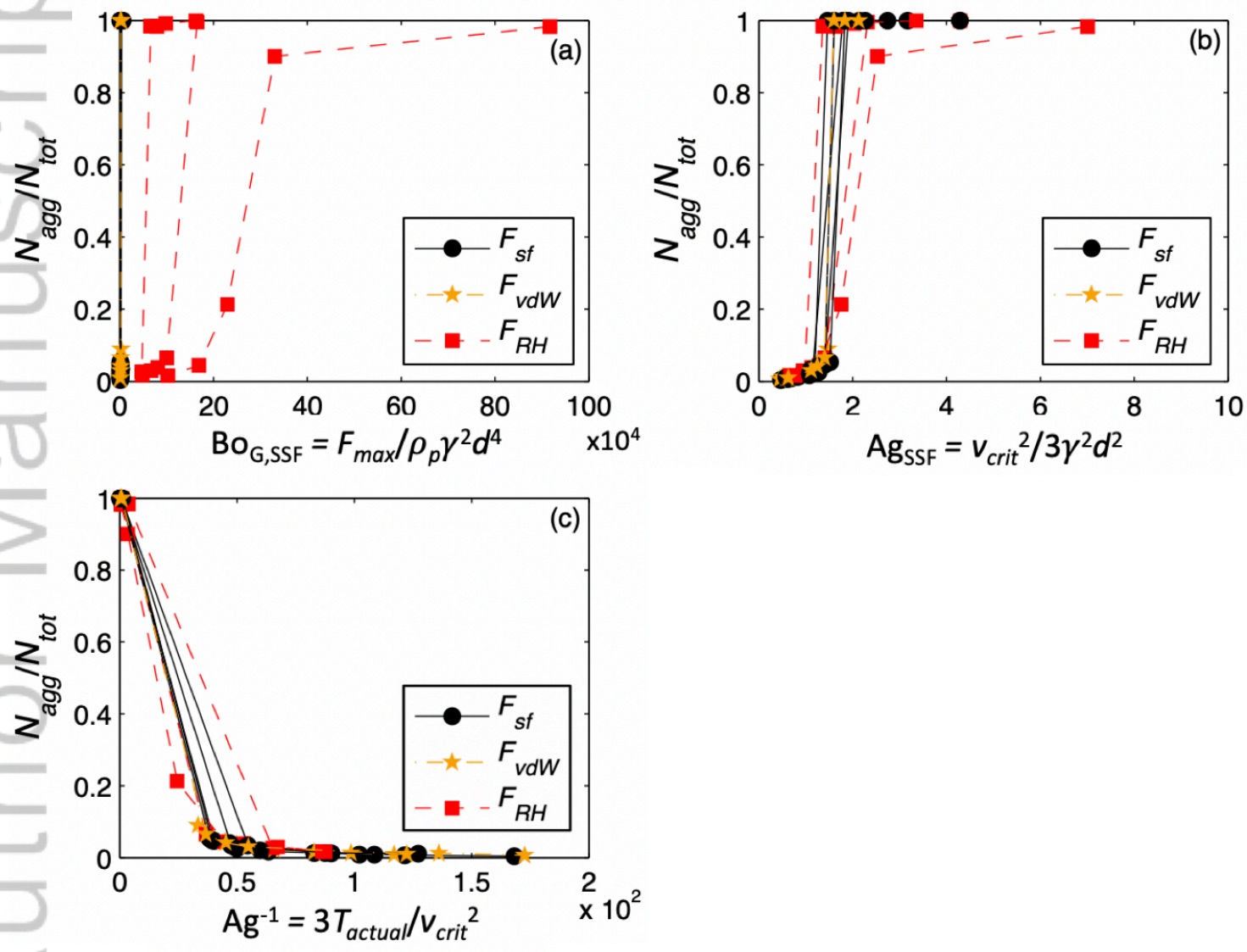




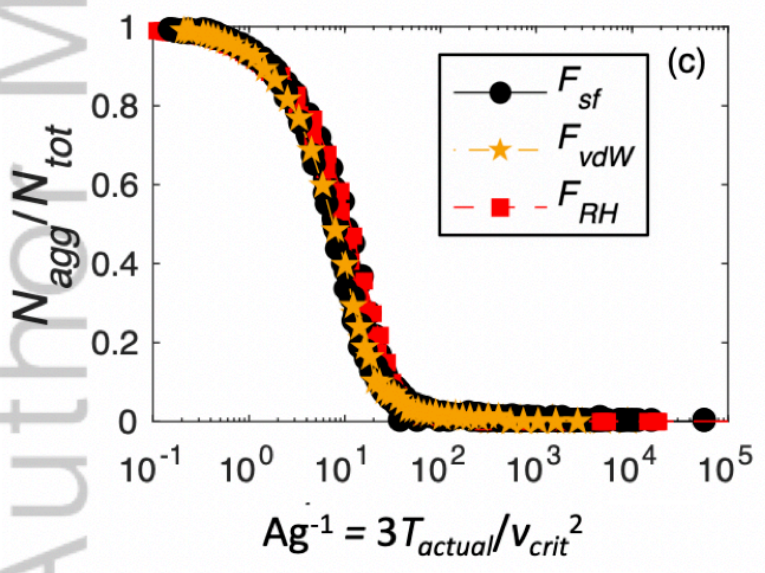
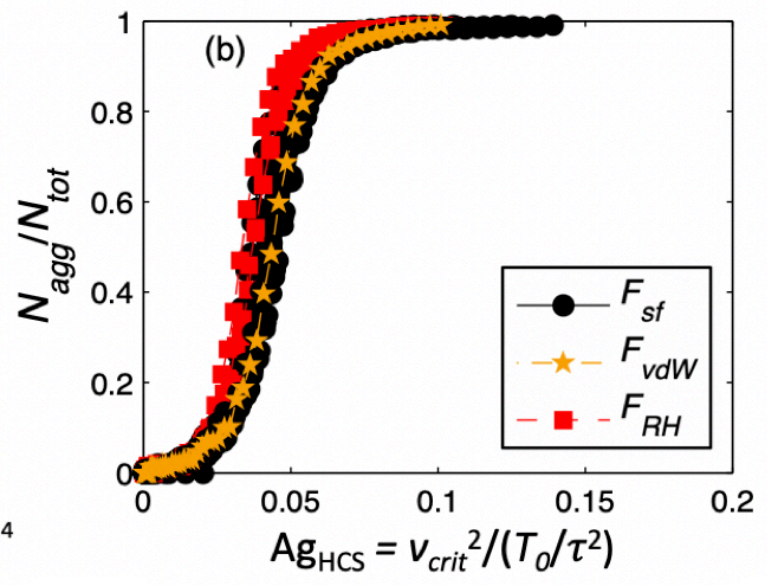
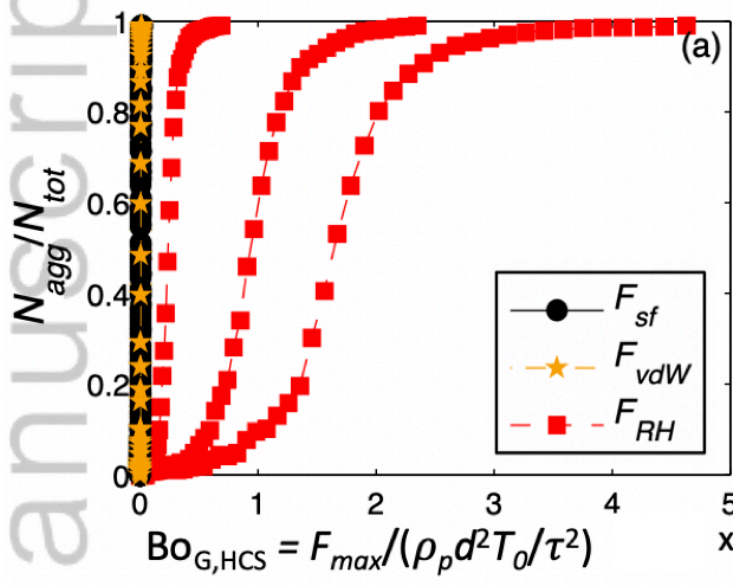
AIC\_17337\_Fig1.tif



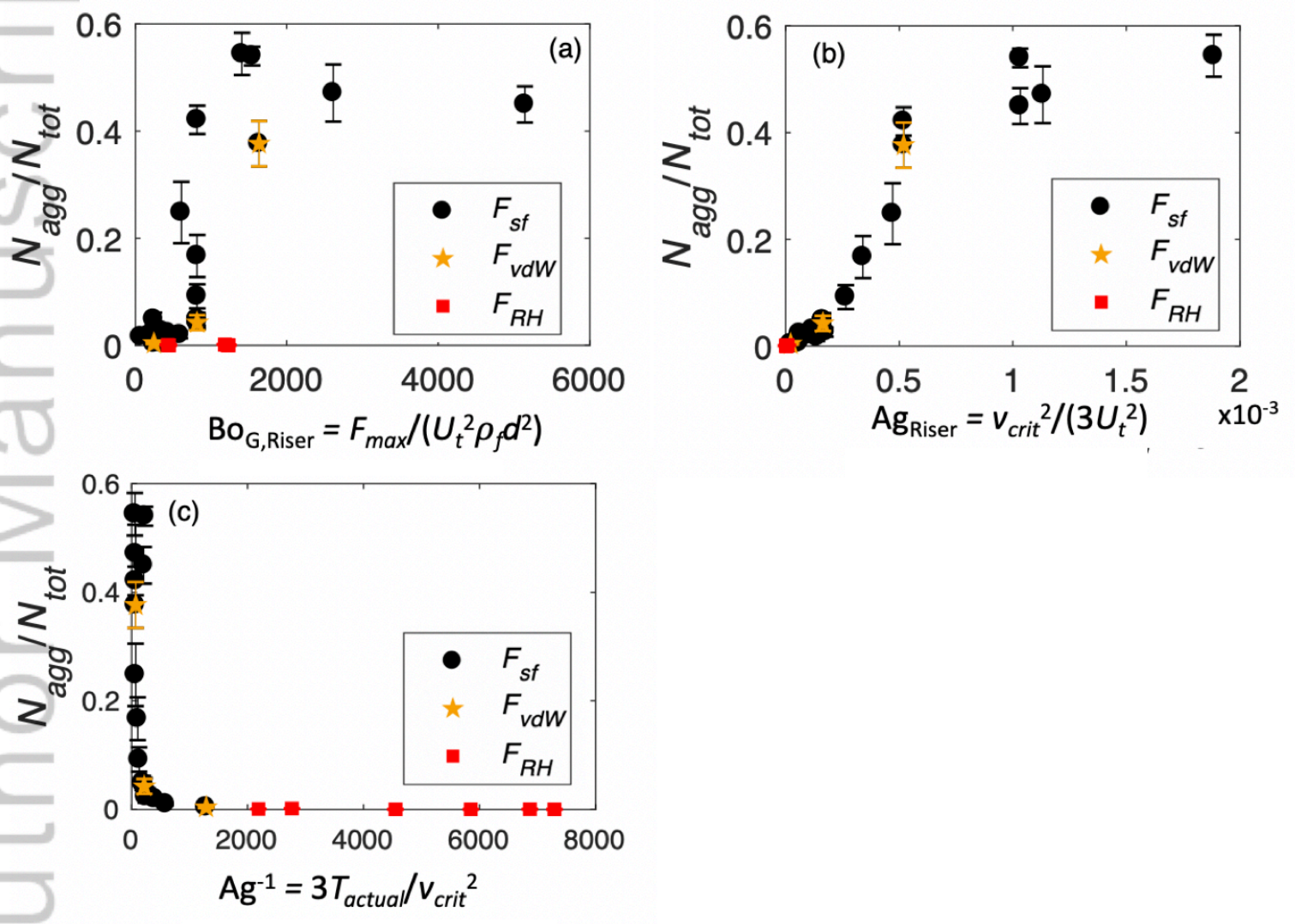
AIC\_17337\_Fig2.tif



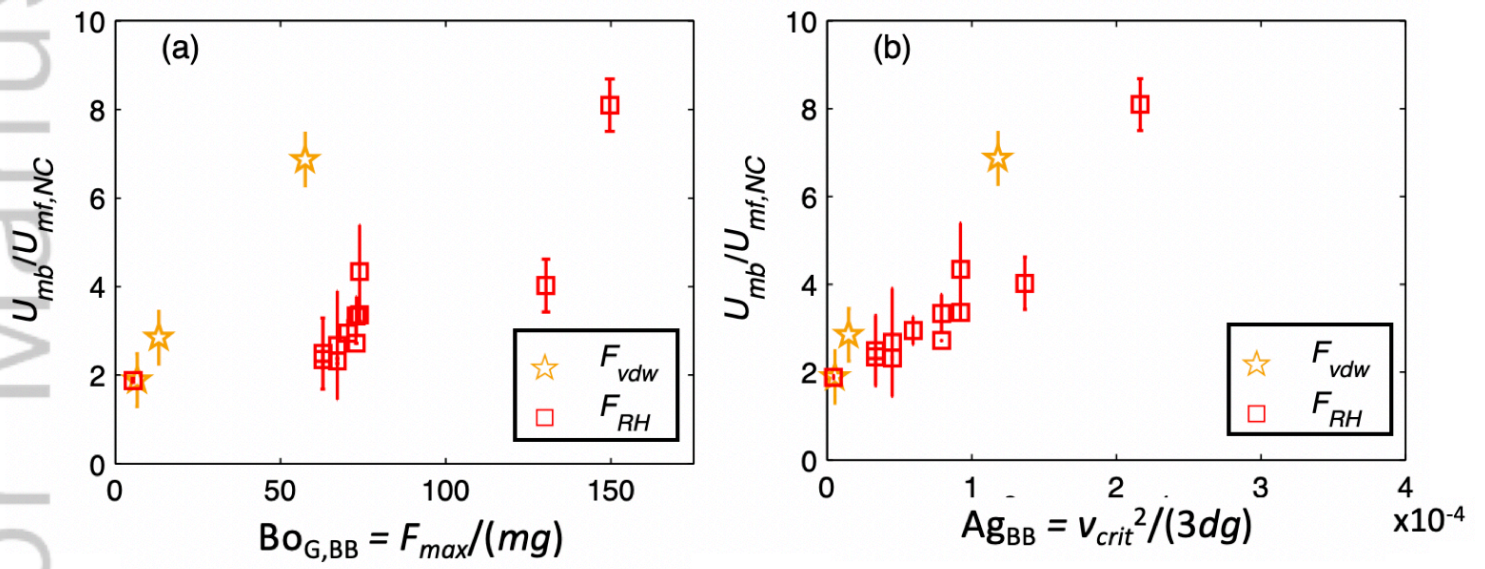
AIC\_17337\_Fig3.tif



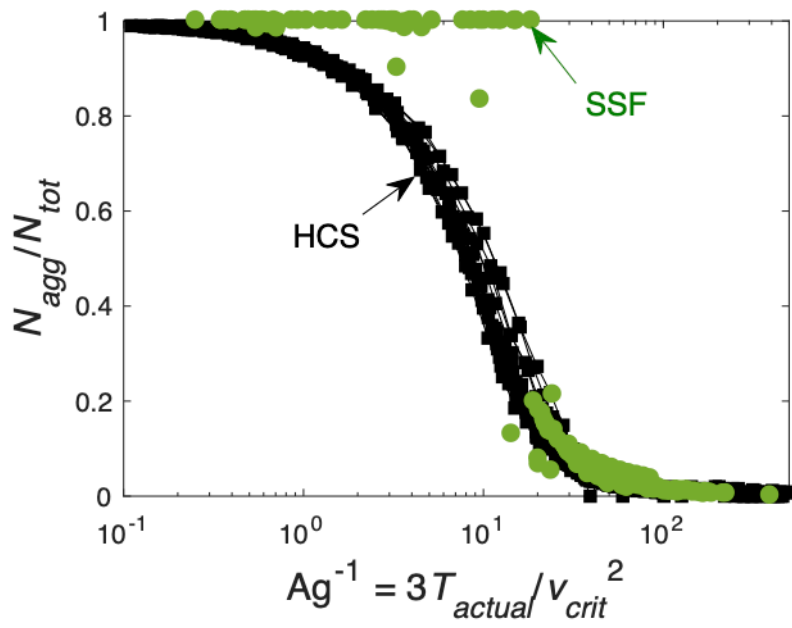
AIC\_17337\_Fig4.tif



AIC\_17337\_Fig5.tif

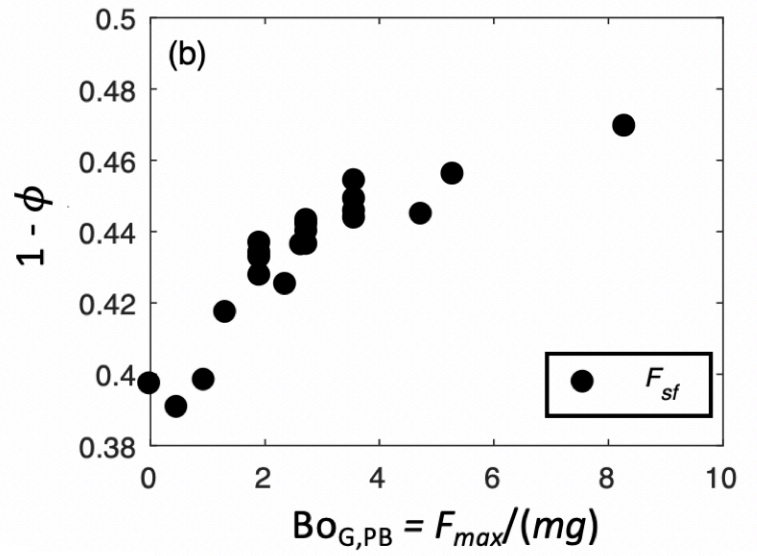
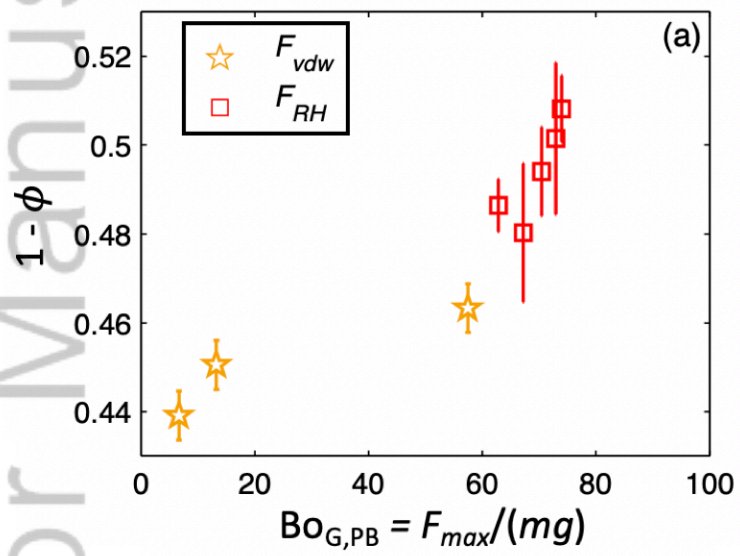


AIC\_17337\_Fig6.tif

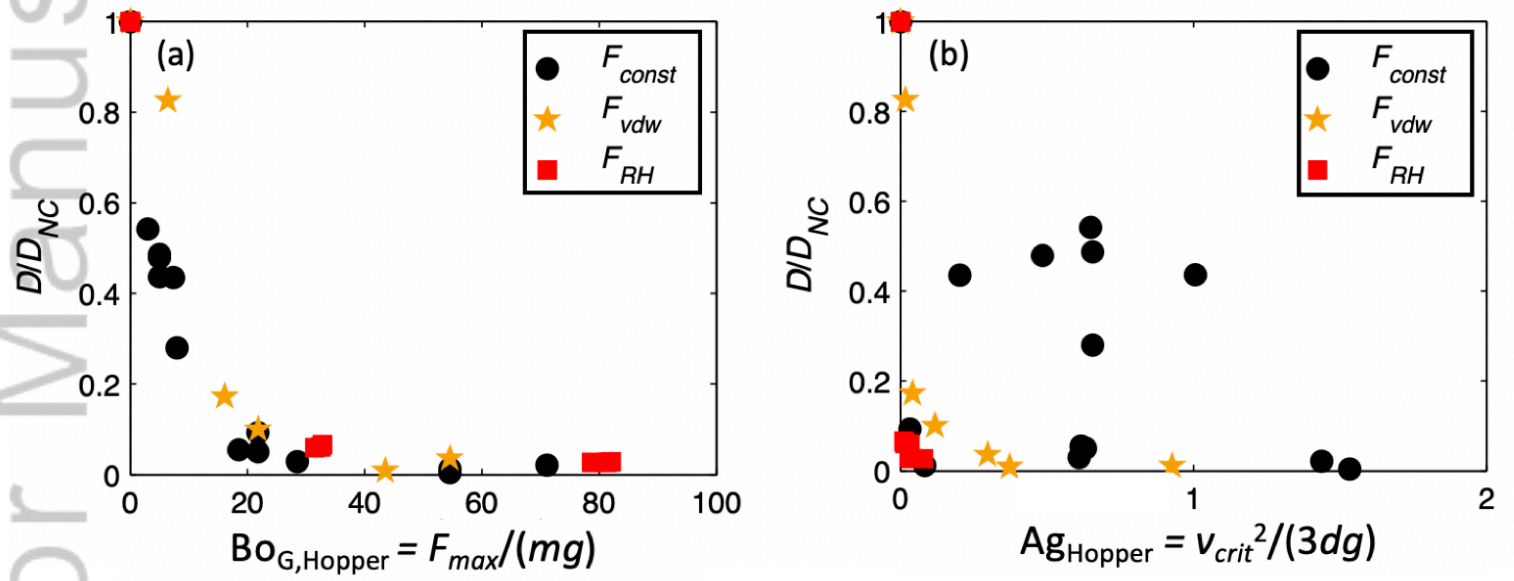


AIC\_17337\_Fig7.tif

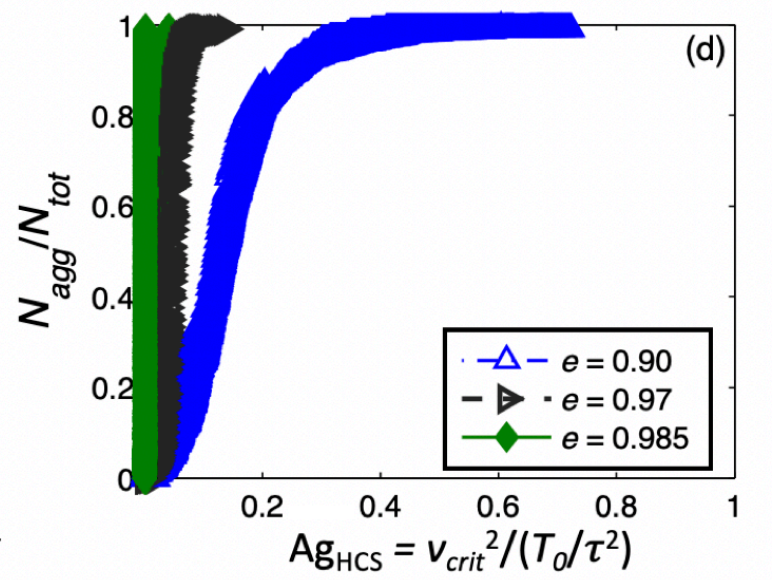
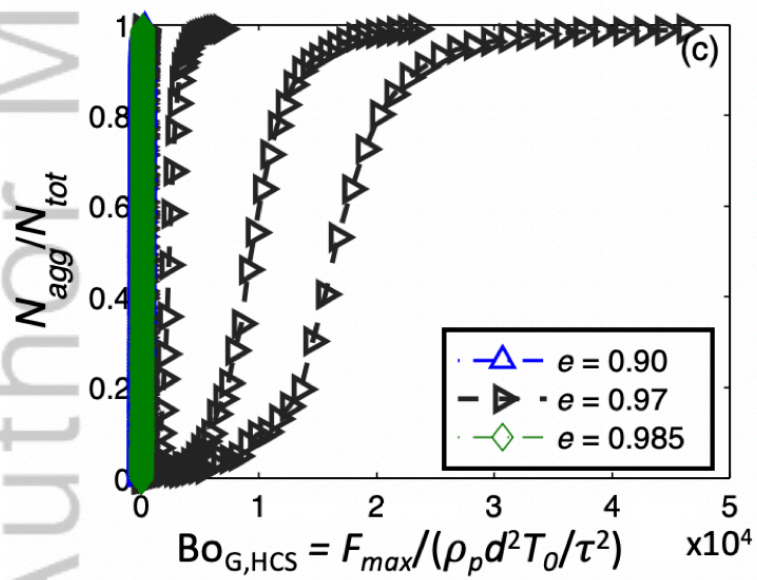
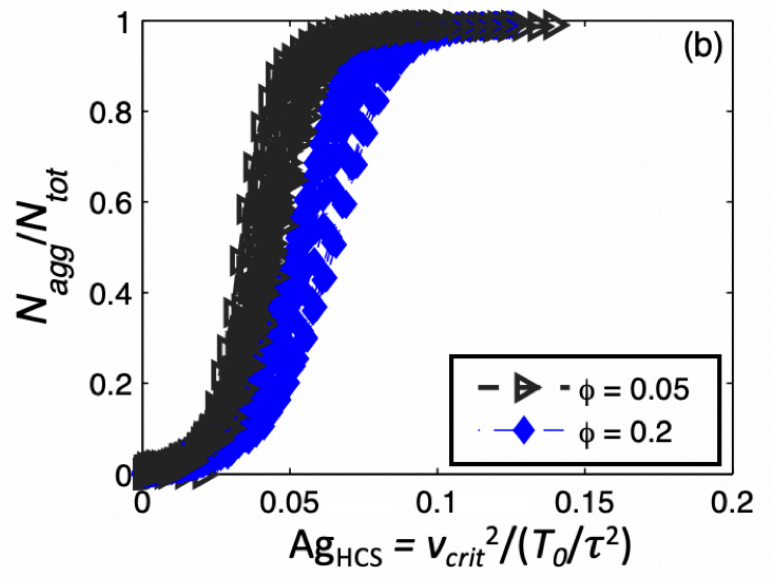
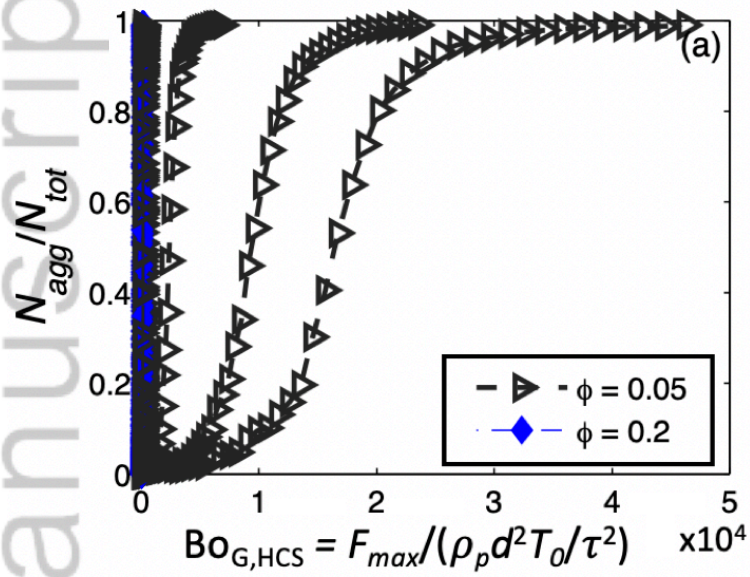




AIC\_17337\_Fig8.tif

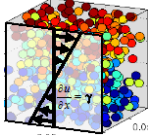
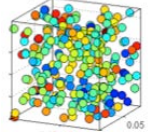


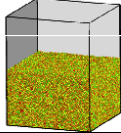

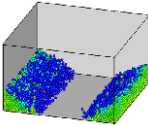


AIC\_17337\_Fig9.tif



AIC\_17337\_Fig10.tif

**Table 1.** Overview of the systems considered.

System		Regime	DEM or Experiment	Sources of cohesion	BOG	Ag
Simple Shear Flow (SSF)		Dilute	DEM	Square-force, humidity and van der Waals	$BO_{G,SSF} = F_{max}/\rho_p\gamma^2d^4$	$Ag_{SSF} = v_{crit}^2/3\gamma^2d^2$
Homogenous Cooling System (HCS)		Dilute	DEM	Square-force, humidity and van der Waals	$BO_{G,HCS} = F_{max}/(T_0\rho_p d^2/\tau^2)$	$Ag_{HCS} = v_{crit}^2/(3T_0/\tau^2)$
Riser		Dilute	DEM	Square-force, humidity and van der Waals	$BO_{G,Riser} = F_{max}/\rho_f U_t^2 d^2$	$Ag_{Riser} = v_{crit}^2/3U_t^2$
Bubbling Bed (BB)		Dilute	Experiment	Humidity and van der Waals	$BO_{G,BB} = F_{max}/mg$	$Ag_{BB} = v_{crit}^2/(3dg)$
Packed Bed (PB)		Dense	DEM	Square-force	$BO_{G,PB} = F_{max}/mg$	N/A
Packed Bed (PB)		Dense	Experiment	Humidity and van der Waals	$BO_{G,PB} = F_{max}/mg$	N/A
Hopper		Dense	DEM	Square-force, humidity and van der Waals	$BO_{G,Hopper} = F_{max}/mg$	$Ag_{Hopper} = v_{crit}^2/(3dg)$

**Table 2.** Equations for solving the condensed capillary force.

Description	Equation	
Capillary Force, <sup>40</sup>	$F_{RH} = 2\pi a_2 \sigma - \pi a_2^2 \eta_{RH} \ln(RH)$	(6)
Kelvin and Laplace- Young Equations, <sup>41</sup>	$-\eta_{RH} \ln(RH) = \sigma(1/a_1 - 1/a_2)$	(7)
Bridge Curvature, <sup>42</sup> $a_1$	$a_1 = r_s[(1+x/2r_s)\sec(\beta) - 1]$	(8)
Bridge Thickness, <sup>42</sup> $a_2$	$a_2 = r_s[(1+x/2r_s)\tan(\beta) - (1+x/2r_s)\tan(\beta) + 1]$	(9)